MinEx CRC Limited
26 Dick Perry Avenue, Kensington, WA, 6151
PO Box 1130, Bentley, WA, 6102, Australia
admin@minexcrc.com.au

ABN: 66 625 533 913

MinEx CRC provides financial support to the value of $1K to promote Honours and Masters by Coursework projects that are aligned with the mission of MinEx CRC and to encourage young researchers toward a career in mineral exploration research. Projects are not restricted to MinEx CRC Participants and Affiliates.

Please note that the content of this thesis has not been subjected to peer-review and subsequent corrections.

Australian Government
Department of Industry, Science and Resources
Cooperative Research Centres Program

The fractionation of copper isotopes in granitic and mafic intrusions: mafic enclaves in the Mannum granite, a case study

Thesis submitted in accordance with the requirements of the University of Adelaide for an Honours Degree in Geology

Oliver Thomas Pring

November 2021

THE FRACTIONATION OF COPPER ISOTOPES IN GRANITIC AND MAFIC INTRUSIONS: MAFIC ENCLAVES IN THE MANNUM GRANITE, A CASE STUDY

COPPER ISOTOPES IN THE MANNUM GRANITE

ABSTRACT

The transfer of material between mantle-sourced magma and evolved magmatic rocks may provide a mechanism for the transportation of metals such as copper, Cu, to the crust. The Mannum granite provides a case study as the A-type granite is synchronously accompanied by mafic enclaves, providing a mafic-felsic interface with differing degrees of mixing/mingling. This mafic-felsic interface shows different mechanisms of transportation such as transport of xenocrysts, compositional rimming (rapakivi feldspars) and change in overall bulk chemistry. Samples of both the granite and mafic enclaves were taken, with a focus on Cu isotope analysis which characterises Cu behaviour between the mafic enclaves and granite and shows whether any copper has been assimilated from a highly fractionated source. This study used petrography, whole rock and mineral major and trace element chemistry and whole rock Cu isotope analysis. Processes such as fractional crystallisation and magma mixing/mingling provide mechanisms for the transfer of material between the granite and the intruding mafic enclaves. There is evidence of the transfer of material in the hybridised zones, particularly the formation of rapakivi feldspars and xenocrysts from both phases. Rare earth element signatures show mineral growth has occurred prior and post injection of mafic magma into the Mannum granite and that magmatic transfer is most applicable to lithophile elements. Cu isotope results show that δ^{65}Cu values generally increase with decreasing copper concentrations and range from -0.12 to 2.34‰. The range of δ^{65}Cu values is in line with those reported in mantle derived rocks and follow Rayleigh fractionation curves. Cu isotope analyses further our understanding of Cu isotope behaviour and can be applied to ore-forming environments. Other stable transition metal isotopes could be paired with Cu isotopes, such as Zn and Fe, to further examine the role of any redox reactions.

KEYWORDS

Copper isotopes, Mannum granite, mafic enclaves, rare earth elements, Rayleigh fractionation, rapakivi feldspars

TABLE OF CONTENTS

LIST OF FIGURES AND TABLES

INTRODUCTION

Understanding the transfer of material through magmatic processes furthers our understanding of the transport of metals to the crust from the Earth's mantle. The transport of metals is key in understanding the concentration of desired metals, such as copper (Cu), and the formation of deposits. Magmatic Cu deposits such as iron-oxide-copper-gold and porphyry copper, form as a result of interaction between the mixing/mingling with other magma and fluids. Sun et al. (2017) proposed that partial melting for subducting slabs mixing and transferring material with the partial melts of mantle peridotites may lead to the formation of porphyry deposits. Zheng et al. (2018) showed that porphyries with associated mafic enclaves have elevated δ^{65}Cu values compared to average felsic rocks. This elevation of δ^{65}Cu values is inconsistent with the formation of sulphides, which often present a negative δ^{65}Cu value (Brzozowski et al., 2020). This indicates that the mixing/mingling between these two phases has caused the enrichment of ^{65}Cu (Zheng et al., 2018).

In this study, the transfer of material between two magmatic phases and its relation to the transport of transition metals from mantle to crust is investigated. The transfer of material in mantle-derived rocks occurs though fractional crystallisation, magma mixing/mingling, and the transfer by magmatic fluids. Fractional crystallisation is the process by which minerals crystallise out of a melt, removing their composition from the melt, and partitioning it into separate compositional mineral phases (Raymond, 1995). Magma mixing/mingling occurs when two melts or partial melts interact; once the two phases reach compositional and thermal equilibrium, they are deemed to have mixed. When two phases interact but remain compositionally separate, with possible mixing along the boundary between the two phases, they are deemed to have mingled (Turner and Foden, 1996; Vernon, 2016; Barnes et al., 2021).

Copper isotope systematics

Copper (Cu) is a reddish transition metal with a density of 8920 kgm^{-3} and it exists in three oxidation states: Cu(0) such as native copper, Cu(I) which commonly occurs in sulphides, and Cu(II) in oxysalts (Moynier et al., 2017; Liu et al., 2021). Cu isotope fractionation occurs during oxidation and to some extent during reduction; fractionation most readily occurs at low temperatures and through fluid interactions (Larson et al., 2003). Cu fractionation can also occur between silicates and sulphides at high temperatures (Liu et al., 2021). Copper has two stable isotopes ^{63}Cu at 69.174% and ^{65}Cu at 30.826% abundance (Shields et al., 1964); the isotopic ratio is expressed as $\delta^{65}Cu$ (relative to a standard reference material – NIST 976) (Liu et al., 2013).

Multi-collector inductively coupled mass spectrometry (MC-ICP-MS) allows precise and accurate measurements of Cu isotope ratios. Solutions of copper prepared through direct digestion and chromatographic purification yield Cu isotope ratios of the whole rock sample (Larson et al., 2003). Copper isotopes are fractionated through both abiotic and biotic processes. Mass-dependent isotopic fractionation predicts the heavier isotope ^{65}Cu will partition into more tightly bonded sites in aqueous species or solids (Bigeleisen and Mayer, 1947; Urey, 1947). The higher atomic mass of ^{65}Cu over ^{63}Cu marginally slows the kinetics of cation exchange for the heavier isotope, thus leading to isotopic fractionation. Cu isotope fractionation occurs most readily in the formation of secondary minerals at low temperature with a $\delta^{65}Cu$ range of 7 to 9 ‰ (Maréchal et al., 1999; Maréchal and Albarede, 2002) In these relatively low energy settings, fractionation is favoured, as the activation energy for exchange is relatively large compared to the thermal energy in the system (Moynier et al., 2017).

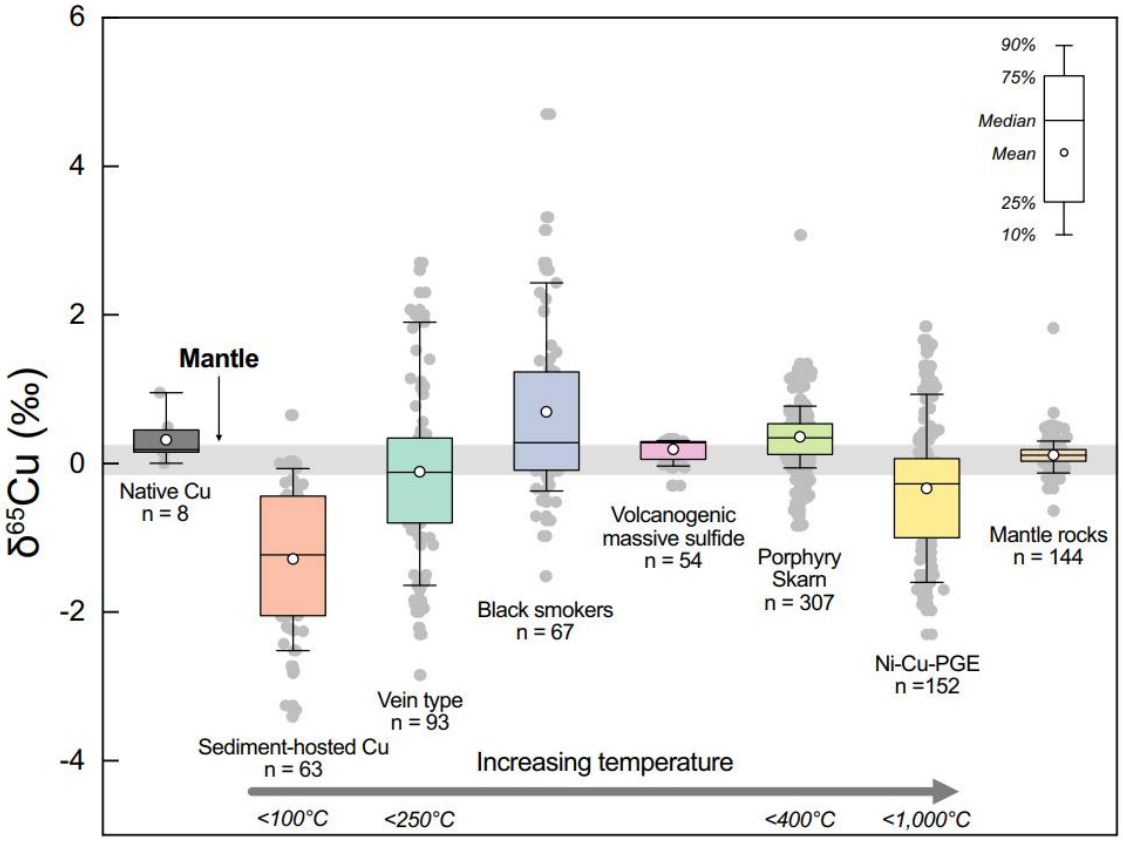

Figure 1: Schematic diagram illustrating the range δ^{65}Cu values for a range of different ore and rock types. Note the relatively narrow spread of values found in mantle-derived rocks. See Brzozowski et al. (2020) for sources of data used in this diagram (after Brzozowski et al., 2020).

The mantle displays a narrow range of copper isotope ratios while hydrothermal systems tend to display much wider ranges of isotopic ratios. Mantle-derived magma typically exhibits δ^{65}Cu values of -0.15 ‰ to 0.18 ‰ while hydrothermally altered mantle-derived rocks exhibit values from –0.64 to +1.82‰ (Liu et al., 2015). As the Mannum granite is a mantle-derived intrusion it is predicted to show a narrow range of δ^{65}Cu values, however if a wide range is found then it can be assumed the Cu content of the Mannum granite is derived from a highly fractionated source such as hydrothermal fluids, assimilation of country rock or a highly fractionated magma system (Liu et al., 2002). Homogenous magmatic-sourced Cu will present a Cu isotope ratio trend, becoming isotopically heavier with decreasing copper concentration following Rayleigh fractionation (Mathur et al., 2012). Rayleigh fractionation

is the evolution of a system as one phase; in this case, the Cu concentration is lowered, resulting in isotopic enrichment (Kendall and Caldwell, 1998).

The Mannum granite

The Mannum granite provides a case study, as it is a mantle-derived A-type granite accompanied by synchronous mafic enclaves, displaying varying degrees of mixing/mingling (Turner and Foden, 1996; Pankhurst et al., 2011). The interactions between the two phases are used as a proxy for large-scale processes involving mantle-derived magma and the crust. The investigation of processes such as fractional crystallisation, assimilation and magma mingling may reveal mechanisms of transfer of metals such as Cu. The degree to which these processes have occurred can be observed through the use of petrography, whole rock major and trace element analysis and rare earth element signature observations (Bea et al., 1994). The Cu isotope fractionation values for the host granite, the mafic enclaves and the intermediate hybridised zones, will be used to understand the degree to which these processes have transferred material from one phase to another, or if the Cu within these rocks has been sourced through assimilation of the upper crust or through interaction with magmatic or hydrothermal fluids.

GEOLOGICAL SETTING

The Mannum granite is located in the eastern Adelaide fold belt, within the Padthaway Suite. It intruded into Late Neoprotozoic early Cambrian meta sediments in the early Ordovician (482.3 ± 4.5 Ma Foden et al., 2006; Pankhurst et al., 2011).

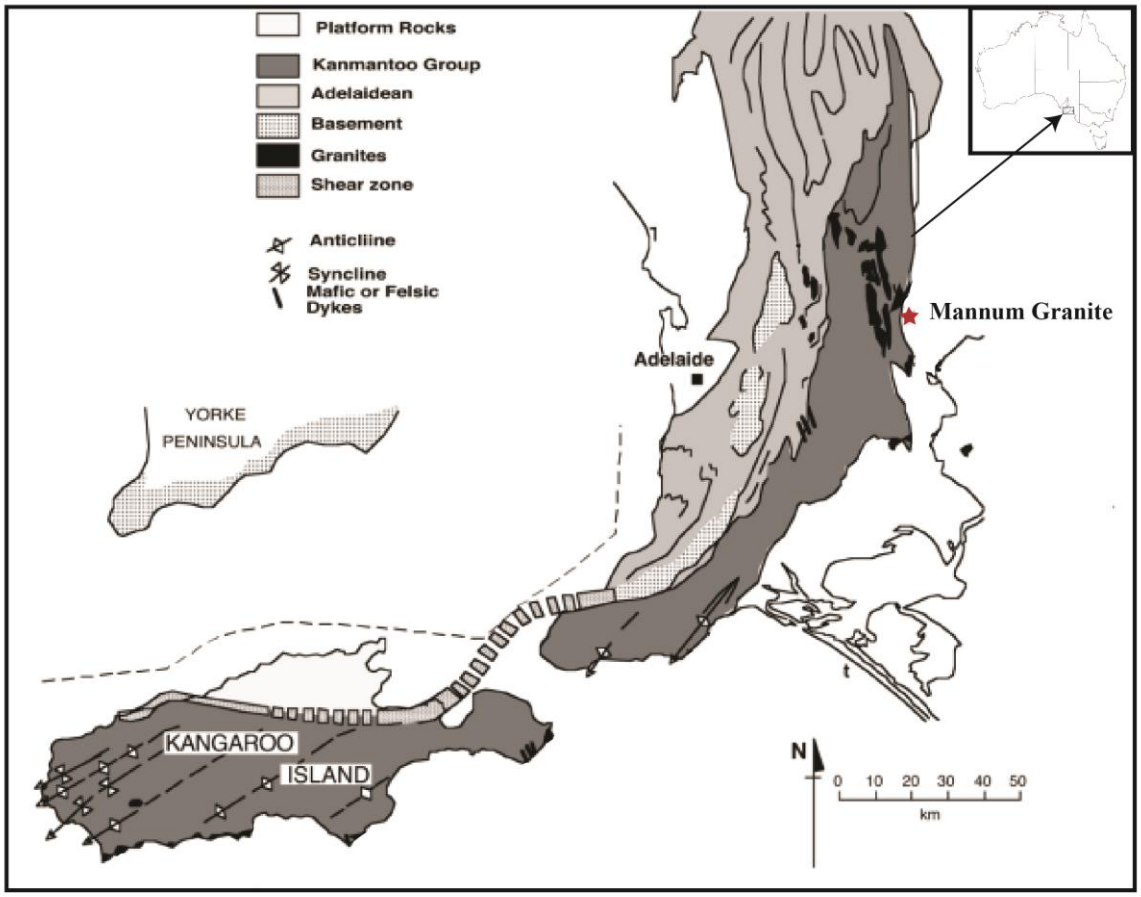

Figure 2: Geological map of Adelaide fold and thrust belt, with the location of the Mannum granite, modified from Foden et al. (2006)

The Padthaway Suite is a series of post-Delamerian granites, volcanics and associated mafic dykes and enclaves (Foden et al., 2006). The Delamerian Orogenic event occurred during the final stages of Gondwana's assembly (Foden et al., 2006). The Padthaway Suite formed due to delamination of a dense moho underplate causing thinning of the lithosphere which allowed mantle upwelling and the formation of 490-470 Ma A-type granites and associated mafic enclaves, intrusions and dykes (Foden et al., 2020). The Mannum granite pluton is

undeformed, roughly circular and 11 km in diameter, and the most prominent outcrop is at the Mannum Quarry on the eastern bank of the River Murray (Turner and Foden, 1996). The Mannum granite originates from an anhydrous magma, indicating a high magma temperature in excess of 930 ^{o}C (Turner and Foden, 1996). The Black Hill gabbro is also a constituent of the Padthaway Suite and represents a mafic melt with similar genetics, and geothermometry reported by Turner (1996) shows a temperature of 1200-1000 ^{o}C. The shape and physical relationship between the enclaves and host Mannum granite indicates the mafic enclaves were an almost liquid magma when injected into the crystal mush of the host granite (Turner and Foden, 1996).

Figure 3: Mannum granite quarry, showing mafic enclaves (dark grey) within host granite (pink-brown).

Turner and Foden (1996) demonstrated that the Mannum granite, and associated enclaves, show initial Sr-isotopic equilibrium indicating fractionation and subsequent mingling from the same parental magma. The Mannum granite is crosscut by a younger basalt dyke, inferred to be closer in composition to the original parental magma (Turner and Foden, 1996). The granite is composed of a medium-coarse syenite-granite and blocks of fine-grained microgranite interpreted by Turner and Foden (1996) to be contaminated margin facies. The

mafic enclaves are tear-drop shaped and range in size from 50 - 5 cm (Turner and Foden, 1996; Frost et al 2001).

The Mannum granite has been extensively studied (e.g., Turner and Foden, 1996; Foden et al., 2002; Foden et al., 2006; Pankhurst et al., 2011; Gibson et al., 2015 Foden et al., 2020) in relation to the timing and cessation of the Delamerian orogeny. As the Mannum granite is a post-tectonic A-type granite, its age (482.3 $\pm$ 4.5 Ma Turner and Foden (2006), 482 $\pm$ 8 Ma Pankhurst et al. (2011), both collected with Rb-Sr isochrons) is interpreted to provide a minimum age for the cessation of the Delamerian orogeny (Foden et al., 2020). Whole rock chemical analyses reported by Turner and Foden (1996) showed a distinct chemical difference between the host granite and the enclaves, and the transition metal composition including Ni, Cr, Sc and V showed enrichment within enclaves compared to the host granite; however, Cu was not reported, in their analysis. Turner and Foden (1996) showed, through decoupling Sr-Nd, that the mafic enclaves are a representation of the parental magma of the Mannum granite.

METHODS

Samples

Samples were collected to represent a full spectrum of phases.

Table 1: Sample names, sample sets, type of sample, use of sample.

Sample	Original no.	Geochemistry sample sets	Sample type	Use
BOUNDARY001	OPMG_001		mafic enclave-granite	petrography
BOUNDARY002	OPMG_002	2A, 2B, 2C	mafic enclave-granite	petrography and geochemistry
HYBRID006	OPMG_006	6A, 6B, 6C	granite-hybridised zone	petrography and geochemistry
ENCLAVE009	OPMG_009		mafic enclaves	petrography and geochemistry
BOUNDARY012	OPMG_012	12A, 12G	granite-mafic boundary	petrography and geochemistry
GRANITE013	OPMG_013		granite	geochemistry
BOUNDARY016	OPMG_016	16A, 16B, 16C, 16D, 16E, 16F	granite-mafic enclave boundary	petrography and geochemistry
BOUNDARY017	OPMG_017		mafic enclave	geochemistry
SOUTHERN DYKE001	OPMGB_001	1A, 1B	Southern mafic enclave/dyke	petrography and geochemistry
MG7 (basalt dyke)	-		dyke	geochemistry

Four enclave boundary (ts = thin section: BOUNDARYts001, BOUNDARYts002, BOUNDARYts012 and BOUNDARYts016), three hybrid (HYBIRDts006A HYBRIDts006B and HYBRIDts006C), one granite (GRANITEts006A), one mafic enclave (ENCLAVEts009) and one southern dyke (SDts001) samples were thin-sectioned by Adelaide Petrographic Inc. The sections were selected for both transmitted and reflected light petrographic analysis. These samples were used as they represent the boundary between the mafic enclaves and the host granite and the differing degrees of hybridisation between them. The mafic enclaves, the granite and the southern mafic dyke were petrographically characterised as they represent each of the phases (or lithologies) without the effects of mixing or mingling.

Whole rock major element analysis

Whole rock major element analysis was conducted by Peter Reiner Wieland at Macquarie University using the following procedure.

For XRF analysis approximately 100 mg of sample was weighed into clean 15 ml Teflon beakers and the mass recorded to four decimal places. Samples were digested using a 1:1 mixture of HF and Teflon distilled HNO_3 at 120°C for 24 hours, then dried down and repeated. Samples were then digested in a mix of 2 ml HF and 10 drops $HClO_4$ overnight and dried down gradually to remove fluoride complexes. A further digest in 6 Mol L^{-1} HCl and then 6 Mol L^{-1} HNO_3 was performed before samples were dissolved in a 2% HNO3/ 0.5% HF solution for analysis.

1:1000 dilutions of each sample were then individually spiked with a 20 µl aliquot of a solution of ^{6}Li, As, Rh, In and Bi in 2% HNO_3. Samples and standards were analysed on an Agilent 7500cs ICPMS. BCR-2 was used as a calibration standard. Standards BIR-1 and BHVO-2 were also analysed in a 1:1000, 1:2000, and 1:5000 dilution.

A blank was subtracted using the 2% HNO_3 0.5% HF rinse.

Whole rock trace element analysis and initially Cu isotope analysis involved the digestion of samples of the various lithologies using the following bomb digestion procedure. Approximately 300 mg of powdered sample were placed into Teflon bombs, with 4 ml of 28 Mol L^{-1} HF and placed on a 140 ^{o}C hotplate, allowed to dry down, adding 1ml of 7 Mol L^{-1} NHO_3 just before the samples dried. After samples had dried 2 ml of 7 Mol L^{-1} NHO_3 was added and allowed to cool. 4 ml of 28 Mol L^{-1} HF was added to the samples and they were capped and sealed in bomb jackets and placed in an oven at 190^{o}C for 94 hours. Bombs were

uncapped and allowed to dry down; 1 ml of 7 Mol L^{-1} NHO_3 was added just before the samples dried. Solid residue was taken up in 5 ml of 2% NHO_3.

For trace element solution ICP-MS analysis the following dilution procedure was used. 1:1000 dilutions were performed; aliquots were taken up into 5 ml of 2% NHO_3. Nineteen samples and two standards (USGS BHVO-2, USGS GSP-2) were analysed using Solution ICP-MS - Agilent 8900x QQQ-ICP-MS at The University of Adelaide (Adelaide Microscopy).

Electron Probe Micro Analyses (EPMA)

Chemical compositions of feldspars, titanite, biotite, magnetite, hornblende and pyrite were determined using a Cameca SXFive Electron Microprobe under standard operating conditions as detailed in Table 2. The standards used for EPMA analysis of silicate and oxide minerals were: Ca and Na (Astimex plagioclase), K (Astimex Sanidine), Mg (Astimex almandine), Ti (P and H block rutile), Si and Al (Astimex albite), Fe (P and H block specularite), Mn (P and H block rhodonite). The standards used for EPMA analysis of sulphides were: S (pyrite), Fe (pyrite), Cu (chalcopyrite), Zn (sphalerite), Co (cobalt), Ni (nickel olivine) and As (arsenopyrite)

Table 2: EPMA operating conditions.

Analysis type	Beam current (nA)	Accelerating voltage (15kV)	Spot size
Silicate composition element analysis	20	15	5
Sulphide composition element analysis	20	13	5

LA–ICP–MS: Trace elements

Trace element analysis of feldspars, titanite, biotite, magnetite, hornblende, pyrite and matrix minerals were undertaken using an Agilent 7900x with attached RESOlution LR 193nm Excimer laser system at Adelaide Microscopy.

Standards used: GSD30, NIST612, STDGL3.

Ion Exchange Chromatography

Digested samples were taken up in 1.5 ml 6 Mol L^{-1} HCl and centrifuged for 5 minutes to separate the solid residue. Samples were passed through a pre-cleaned column with anion exchange resin (Bio-Rad AG® 1-X8 200–400 mesh), using the steps outlined in Table 3.

Table 3: Column chromatography procedure for a column with 1 ml AG1-X8 (200-400 mesh) resin.

Step	Solvent	Eluent
Cleaning	3 mol L-1 HNO3	10ml new resin, 15 ml reusing resin, into waste beaker
Cleaning	Milli-Q H2O	10ml new resin, 15 ml reusing resin, into waste beaker
Cleaning/ equilibration	6 mol L-1 HCl	10ml new resin, 15 ml reusing resin, into waste beaker
Sample load	6 mol L-1 HCl	1.5 ml into waste beaker
Elute matrix	6 mol L-1 HCl	7.5 ml into waste beaker
Collect sample into previous digestion vessel	6 mol L-1 HCl	18ml into collecting vial

On subsequent runs, samples were put through the columns twice to achieve higher purity, removing elements such as Ti and Fe which may interfere with the recorded Cu isotopic ratios. The first run was performed with a widened collection volume outlined in Table 4, eluting the matrix with 6 ml of 6 Mol L^{-1} HCl, followed by 22 ml 6 Mol L^{-1} HCl for collection. The second run was performed with 7.5 ml of 6 Mol L^{-1} HCl followed by 18 ml 6 Mol L^{-1} HCl (Table 3). Standard BCR-2 was run through columns a third time to remove any possible transition metals causing interference in Cu isotope analysis.

Table 4: Column chromatography expanded collection run.

Step	Solvent	Eluent
Cleaning	3 mol L-1 HNO3	10ml new resin, 15 ml reusing resin, into waste beaker
Cleaning	Milli-Q H2O	10ml new resin, 15 ml reusing resin, into waste beaker
Cleaning/ equilibration	6 mol L-1 HCl	10ml new resin, 15 ml reusing resin, into waste beaker
Sample load	6 mol L-1 HCl	1.5 ml into waste beaker
Elute matrix	6 mol L-1 HCl	6 ml into waste beaker
Collect sample into previous digestion vessel	6 mol L-1 HCl	22ml into collecting vial

Multi-Collector Inductively Coupled Plasma Mass Spectrometry (MC-ICP-MS)

Copper isotopic determination was performed using a ThermoFinnigan Neptune Multi-Collector (MC-ICP-MS) at CSIRO/The University of Adelaide Waite campus. Sample solutions were introduced by auto sampler under 'dry' plasma using a spray chamber. Samples and standards were diluted to 200 ppb and measured for three blocks of 60 cycles. Samples were analysed in low-resolution mode with the Faraday cup configuration in Table 5. Cu isotopic data are reported in standard δ-notation (per mil ‰) relative to a standard reference material:

$$\text{NIST 976 } \delta^{65}\text{Cu} = 65Cu/63\text{Cu sample}/\ 65\text{Cu}/63\text{Cu NIST 976} - 1 \times 1000.$$

Standard sample bracketing was used to account for machine drift and a 200 ppb Ga spike was used to correct for mass bias.

Table 5: Configuration of Faraday cup with 1011 Ω resistors for Cu isotope analysis on the ThermoFinnigan Neptune MC-ICP-MS.

Cup	L4	L3	L2	L1	C	H1	H2	H3	H4
Isotope	^{63}Cu	^{64}Zn	^{65}Cu	^{66}Zn	^{67}Zn	^{68}Zn	^{69}Ga	^{70}Zn	^{71}Ga

RESULTS

Petrography

The Mannum granite can be subdivided into six seemingly distinct phases: the host granite, intermediate hybridised zone, the mafic enclaves and southern dyke, the basalt dyke and microgranite. Examples of the spatial distribution of these lithologies are shown in Figure 4 (A and B).

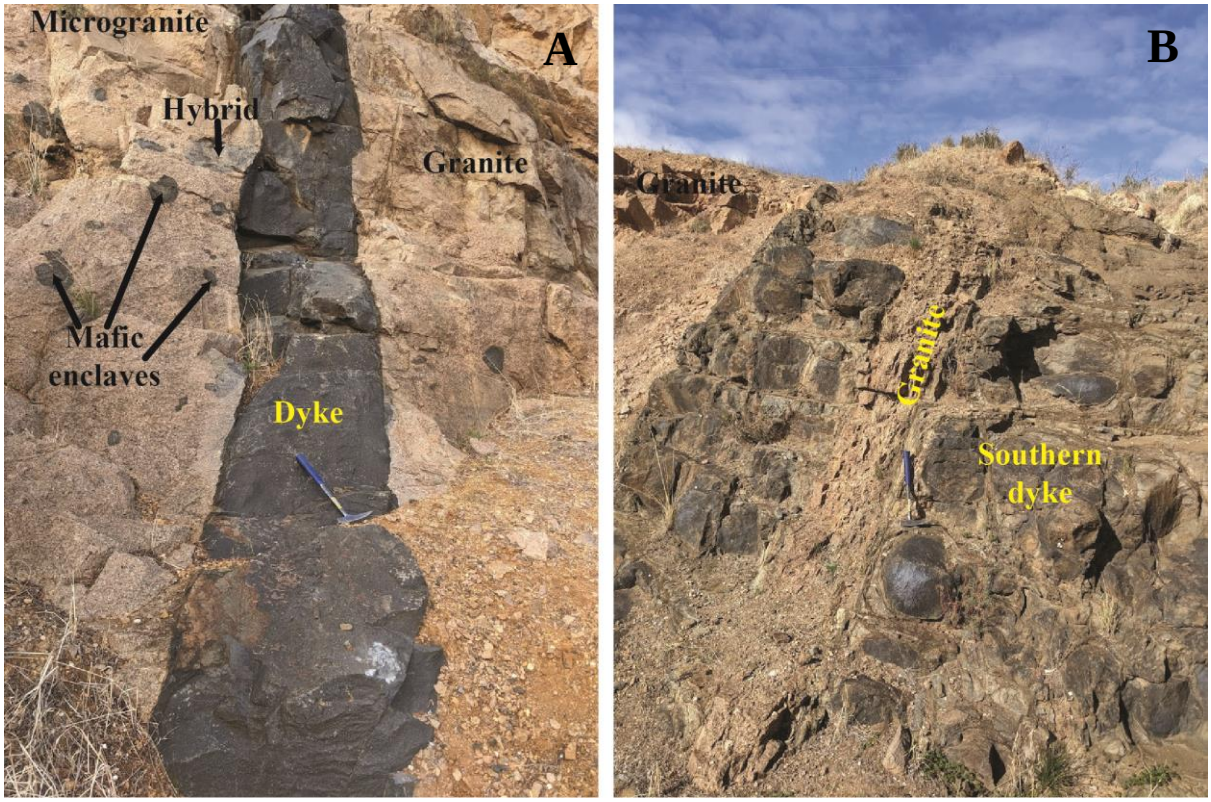

Figure 4: Different phases of the Mannum granite. (A) The Mannum dyke, fine-grained intrusive dark basalt, mafic enclaves dark grey to grey, the hybridised phase grey to light grey, granite and micro granite in beige. (B) shows the southern dyke which is contemporaneous with the mafic enclaves and shares the same mineral composition and displays mingling textures with the host granite.

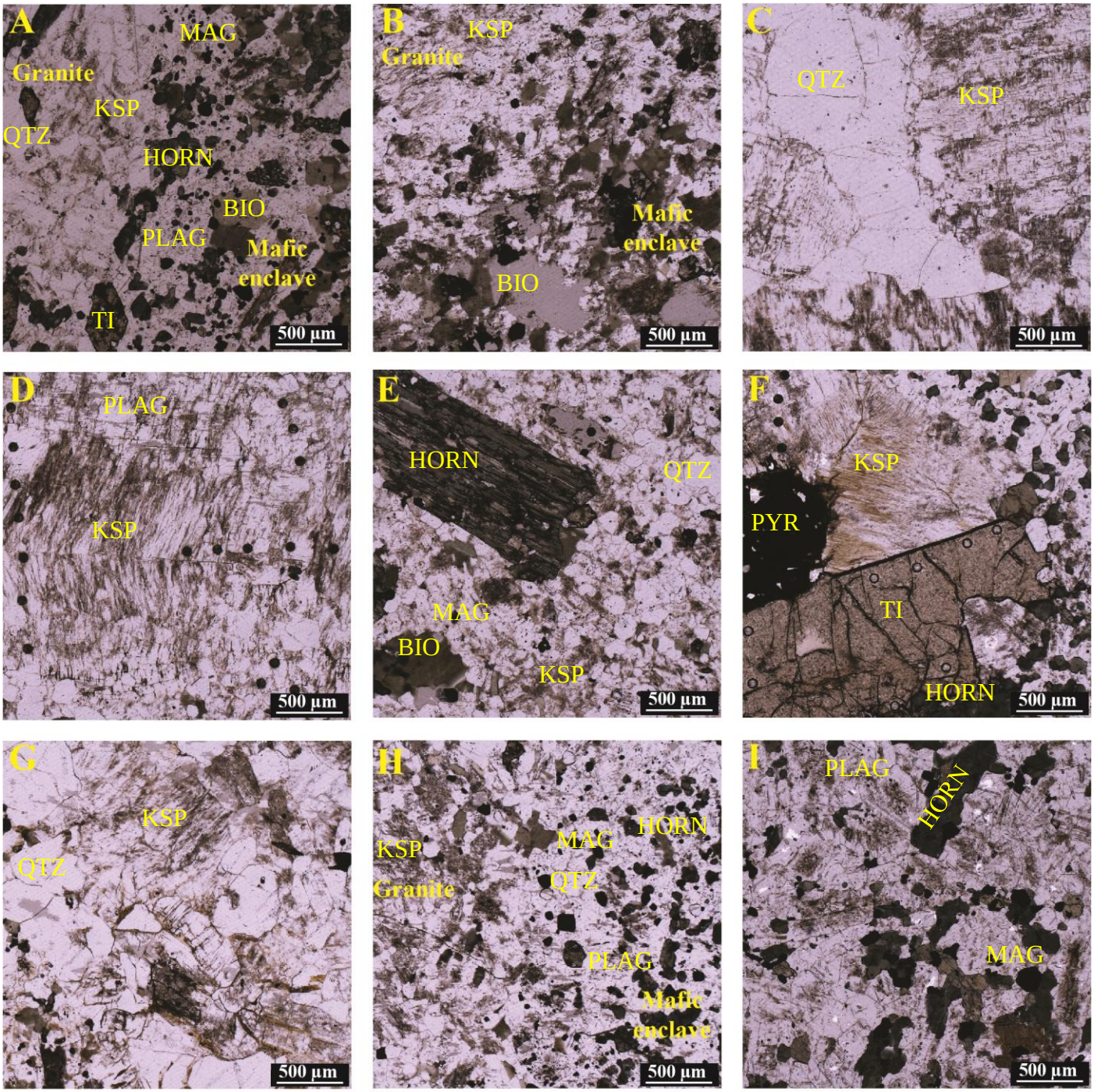

Figure 5: Photomicrographs of Mannum granite samples in plane-polarised light. (A) BOUNDARYts001 mafic enclave bounding host granite with phenocrysts of alkali feldspar and quartz, with minor biotite and titanite. The mafic enclave is dominated by plagioclase, biotite and hornblende with minor magnetite. (B) BOUNDARYts002 mafic enclaves bounding host granite, with the same mineral composition to BOUNDARYts001. (C) HYBRIDts006A host granite near to a hybrid zone, comprising quartz and alkali feldspar. (D) HYBRIDts006B intermediate hybrid zone, rapakivi texture. (E) HYBRIDts006C intermediate hybrid zone, with large xenocryst hornblende crystals, rapakivi texture, quartz and biotite. (F) ENCLAVEts009: mafic enclave, comprising hornblende and plagioclase with large titanite crystals often associated with KSP. (G) BOUNDARYts012 granite mafic enclave boundary, focused on the felsic phase, showing a lack of mixing/mingling. (H) BOUNDARYts0016, enclave-granite boundary, displaying anhedral alkali feldspar, quartz and biotite, bounding hornblende, plagioclase, magnetite. (I) SDts001, southern dyke thought to be contemporaneous with the host granite, comprising plagioclase, magnetite and hornblende.

The mafic enclaves (Figures 5 A, B, F, H, I) are dominated by small anhedral to subhedral 100 µm scale plagioclase feldspar and hornblende crystals. Larger crystals (up to 2 mm) of plagioclase and hornblende are also present with subhedral edges and show a more degraded texture, often showing zonal rims of differing composition. Biotite is also prevalent ranging from 0.2-1 mm. The mafic enclaves also have minor magnetite and pyrite. Figure 5F shows a large anhedral pyrite crystal between the titanite and alkali feldspar. This occurrence of large 1-5 mm titanite, alkali feldspar and smaller pyrite crystals is prevalent throughout sample ENCLAVEts009, however it was not observed in other enclave samples. These titanite, alkali feldspar occurrences possess internal euhedral edges, an internal anhedral edge with pyrite, and external anhedral edges, shown in Figure 5F.

The host granite (Figure 5C, G) comprises phenocrysts of euhedral alkali feldspar (5-10 mm), with a cloudy appearance due to exsolution, euhedral quartz (1-5 mm) and anhedral biotite (1-3 mm), with minor magnetite and titanite (<0.5 mm) and very rare pyrite (<0.5 mm). In samples bounding mafic enclaves some pyrite is present, often as small anhedral crystals, however in BOUNDARYts016 there is a large subhedral pyrite crystal (1mm). Rapakivi feldspars are also found in the host granite and their frequency is dependent on proximity to mafic enclaves.

The hybrid phase is composed of alkali/rapakivi feldspar (5-10 mm), and quartz phenocrysts (1-3 mm) and anhedral biotite crystals (1-3 mm). Minor magnetite and pyrite (<0.5 mm) are also present, along with hornblende xenocrysts (Figure 5E). The width of the plagioclase rims on alkali feldspar varies greatly even within a single sample from 10 – 100 µm, and the rims are less cloudy compared to the alkali feldspar core indicating less exsolution.

Major elements

Whole rock major element data are summarised in Table 6, and Harker plots of major elements compared to SiO_2 are given in Figure 6. The orange circle in the plots in Figure 6 represents the mafic dyke, which generally lies off the trend line (K_2O, Fe_2O_3 and Al_2O_3 being exceptions). Oxides: TiO_2, Fe_2O_3 (Fe is present as Fe^{3+} and Fe^{2+}), MgO, CaO and MnO all display decreasing trends with increasing SiO_2. Al_2O_3 decreases slightly in felsic samples, Na_2O initially increases with SiO_2, peaks at 57-58% SiO_2, then decreases. The amount of Al_2O_3 decreases from a high of 15 wt% in mafic enclaves to a low of 13 wt% in felsic samples. Table 7 compares data reported by Turner and Foden (1996) specifically for MG7 which were reanalysed for this study and show only an average percent difference of 0.16% between the two analyses.

Table 6: Whole rock major element results for sample sets.

Sample	SiO_2	Al_2O_3	Na_2O	MgO	P_2O_5	TiO_2	CaO	K_2O	Fe_2O_3	MnO	Total
MG7	46.9	16.0	3.61	7.13	0.37	1.97	9.65	0.71	12.15	0.24	98.8
HYBRID006B	69.4	13.3	4.03	0.65	0.11	0.45	1.32	4.74	2.62	0.08	96.8
HYBRID0016B	66.9	13.7	4.78	1.33	0.36	0.85	2.38	3.28	4.90	0.14	98.6
HYBRID0002A	62.6	13.8	4.10	2.20	0.35	1.28	3.06	4.00	6.24	0.18	97.8
ENCLAVE016D	58.3	15.1	6.13	2.57	0.76	1.52	4.31	1.40	8.42	0.25	98.8
ENCLAVE016E	57.9	15.0	6.20	2.68	0.75	1.57	4.34	1.36	8.52	0.25	98.6
ENCLAVE016F	56.7	15.2	6.22	2.86	0.82	1.63	4.50	1.41	9.16	0.27	98.7
ENCLAVE017A	48.3	14.3	4.73	5.02	0.66	2.47	6.88	1.72	12.90	0.30	97.3
ENCLAVE016C	57.2	14.9	6.06	2.64	0.74	1.52	4.26	1.36	8.49	0.25	97.4
ENCLAVE002B	57.4	14.4	4.62	3.18	0.49	1.73	4.62	3.05	8.50	0.36	98.4
ENCLAVE002C	57.3	14.4	4.50	3.16	0.47	1.72	4.70	3.31	8.60	0.46	98.6
ENCALAVE 009	55.3	14.8	5.02	3.68	0.42	1.67	5.80	3.11	8.70	0.29	98.8
SOUTHERN DYKE/ENCLAVE001A	56.5	14.9	4.84	3.06	0.76	1.76	5.56	1.83	9.55	0.15	98.9
SOUTHERN DYKE/ENCLAVE001B	56.7	14.9	4.72	3.02	0.74	1.77	5.46	1.90	9.29	0.15	98.6
BOUNDARY012A	69.6	13.0	4.46	1.29	0.16	0.77	1.77	3.26	4.48	0.10	98.9
GRANITE013A	70.4	14.0	4.13	0.62	0.10	0.45	1.23	5.21	2.42	0.07	98.6
GRANITE016A	72.2	13.8	3.92	0.40	0.06	0.32	0.98	5.59	1.75	0.06	99.1
HYBRID006A	69.0	13.6	4.02	0.77	0.13	0.53	1.44	4.88	3.13	0.09	97.6
GRANITE012G	72.0	13.8	3.96	0.41	0.07	0.36	0.77	5.39	2.15	0.03	99.0

Table 7: Major element data sample MG7: comparison of current data to Turner and Foden (1996).

	SiO_2	Al_2O_3	Na_2O	MgO	P_2O_5	TiO_2	CaO	K_2O	Fe_2O_3	MnO	Total
2021	46.938	16.046	3.614	7.134	0.37	1.968	9.648	0.71	12.152	0.242	98.822
Turner and Foden 1996	46.61	15.93	3.47	7.37	0.37	2.03	9.62	0.75	12.33	0.23	98.71

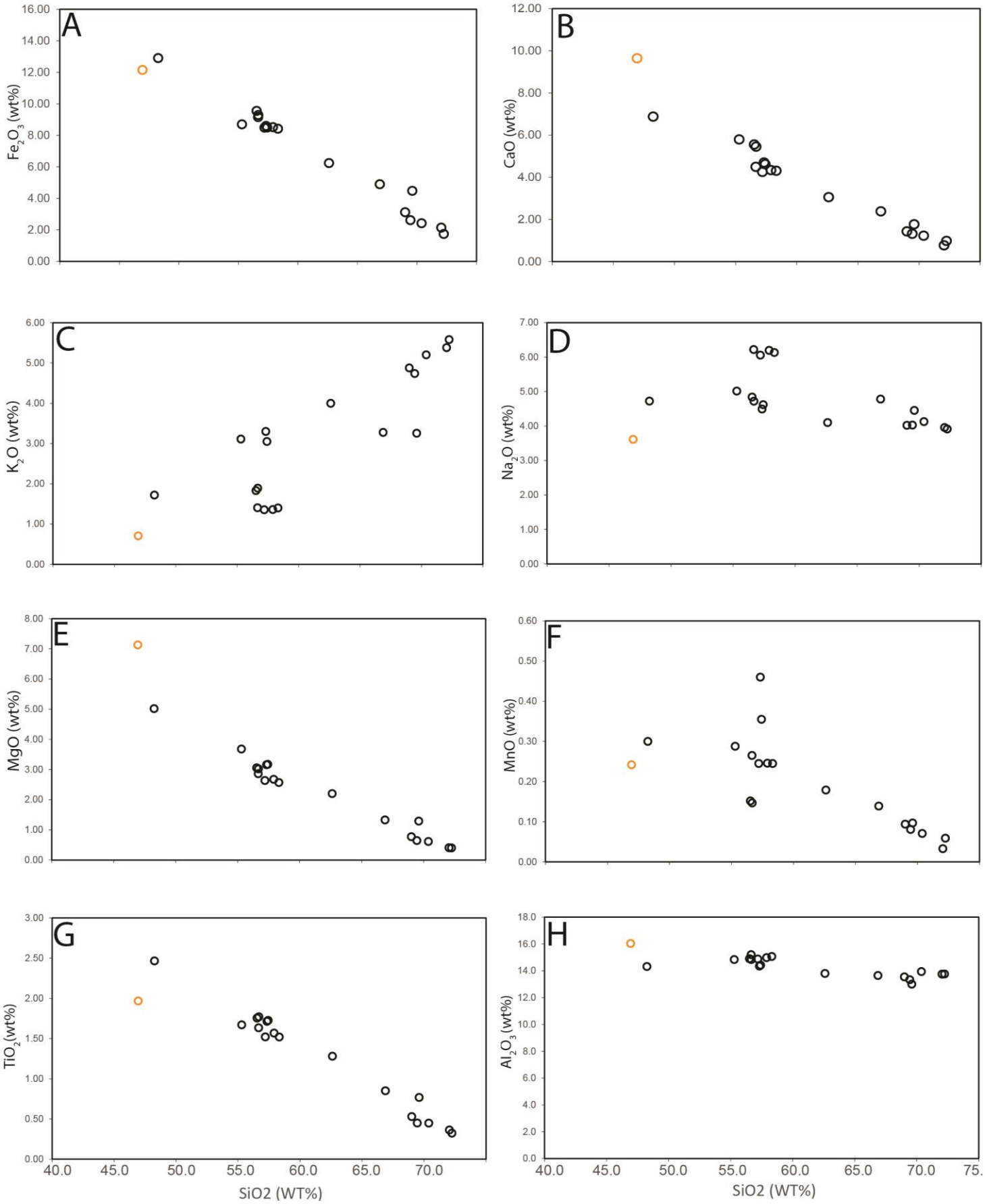

Figure 6: Harker plots of whole rock major elements. (A) Fe_2O_3 and SiO_2, (B) CaO and SiO_2, (C) K_2O and SiO_2, (D) Na_2 and SiO_2, (E) MgO and SiO_2, (F) MnO and SiO_2, (G) TiO_2 and SiO_2, (H) Al_2O_3 and SiO_2.

Electron probe micro analysis

EPMA analysis shows major element composition of individual crystals, and the changes in mineral composition due to the introduction of magma of a different composition. Figure 7A shows a rapakivi feldspar in sample HYBRID006B. Rims of the crystal show a plagioclase composition while the core has an alkali feldspar composition; the change of composition is abrupt, indicating a distinct change in local magma chemistry. An inclusion of plagioclase feldspar is also present within the crystal, possibly a former xenocryst from a less evolved magma. Figure 7B shows an alkali feldspar xenocryst within a mafic enclave, contacting titanite and pyrite. This crystal lacks a rapakivi rim; the alkali feldspar crystal is anhedral and much larger than the surrounding hornblende and plagioclase crystals, suggesting that this crystal formed before the mafic magma mingled within the host granite. EPMA analysis of titanites shows no chemical zoning of titanite in all phases titanite.

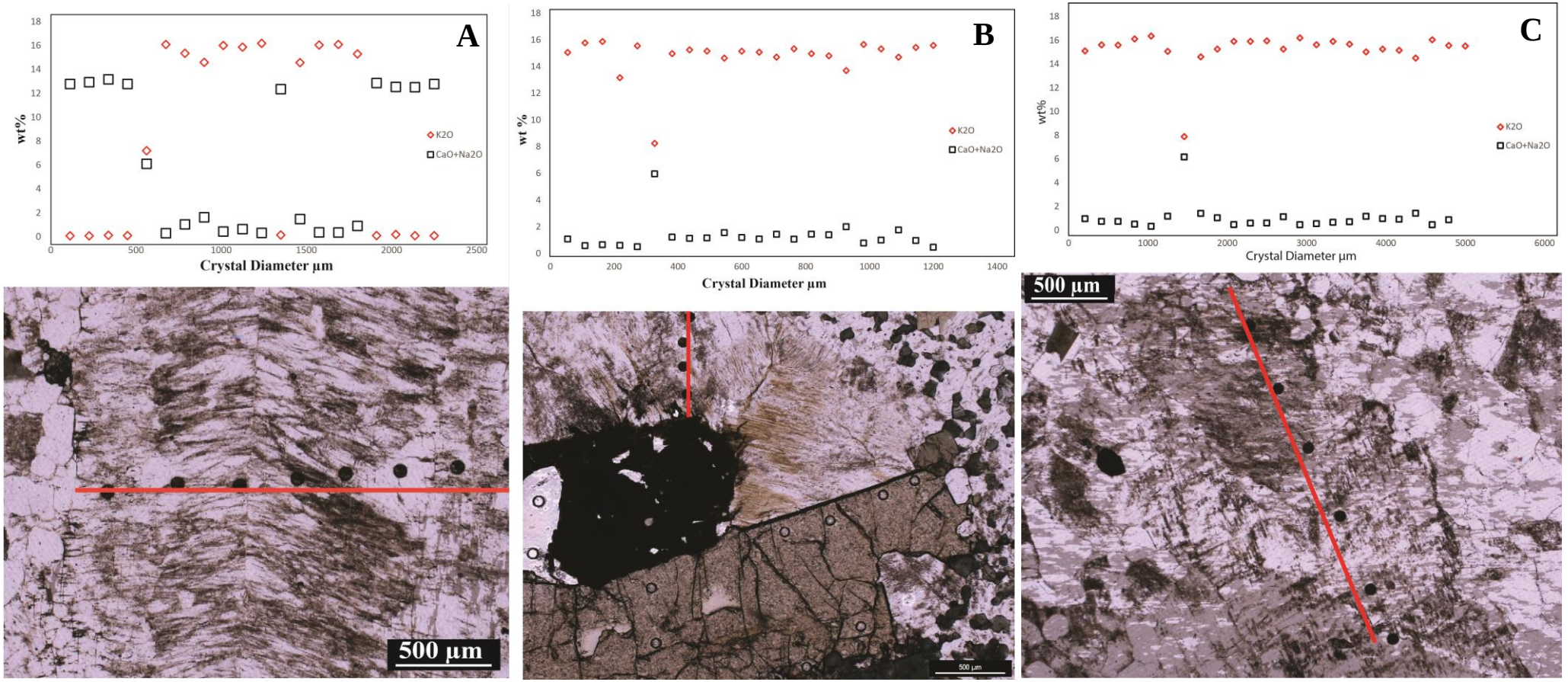

Figure 7: EPMA traverses of individual crystals in the Mannum granite. (A) rapakivi feldspar crystal in HYBRIDts006B, crystal composition change with diameter is modelled, K_2O WT% and Na_2O+CaO WT% are shown. The red line shows the extent of the traverse analysis. (B) alkali feldspar crystal in ENCLAVEts009, crystal composition change with diameter is modelled, K_2O WT% and Na_2O+CaO WT% are shown. The red line shows the extent of the traverse analysis. (C) alkali feldspar crystal in BOUNDARYts016, crystal composition change with diameter is modelled, K_2O WT% and Na_2O+CaO WT% are shown. The red line shows the extent of the traverse analysis.

Whole rock and mineral rare earth element signatures

Figure 8 shows whole rock REE signatures from trace element data from Solution ICP-MS. Figures 9 and 10 respectively show titanite and hornblende REE signatures of individual minerals from LA-ICP-MS analysis.

Figure 8 displays REE signatures and shows all samples following the same general trend. Figure 8A shows that the three most enriched in REEs are all from sample series 16, BOUNDARY016F, BOUNDARY016E and BOUNDARY016C, which are all from the mafic enclave section of the sample, near the boundary with the host granite. The mafic dyke sample, MG7, presents a very different pattern from all other samples, showing an almost straight trend depleting towards the HREEs; other samples show an initial depleting trend to Eu then a consistent trend for HREEs. Granite samples in Figure 8B show a consistent pattern with a significant negative Eu anomaly, with small variation in overall REE enrichment. Hybrid samples (Figure 8C) show a slight variation in pattern with LREEs and a small variation in overall REEs. The Eu anomaly becomes less pronounced as samples become more mafic in composition, with samples ENCLAVE009, ENCLAVE017 and ENCLAVE016D showing little to no negative Eu anomaly (Figure 8D). Sample set 016 (Figure 8E) shows a wide range in REE signatures with 16E and F presenting the highest La and Lu concentrations, while sample 16A is generally low in all REEs compared to other samples.

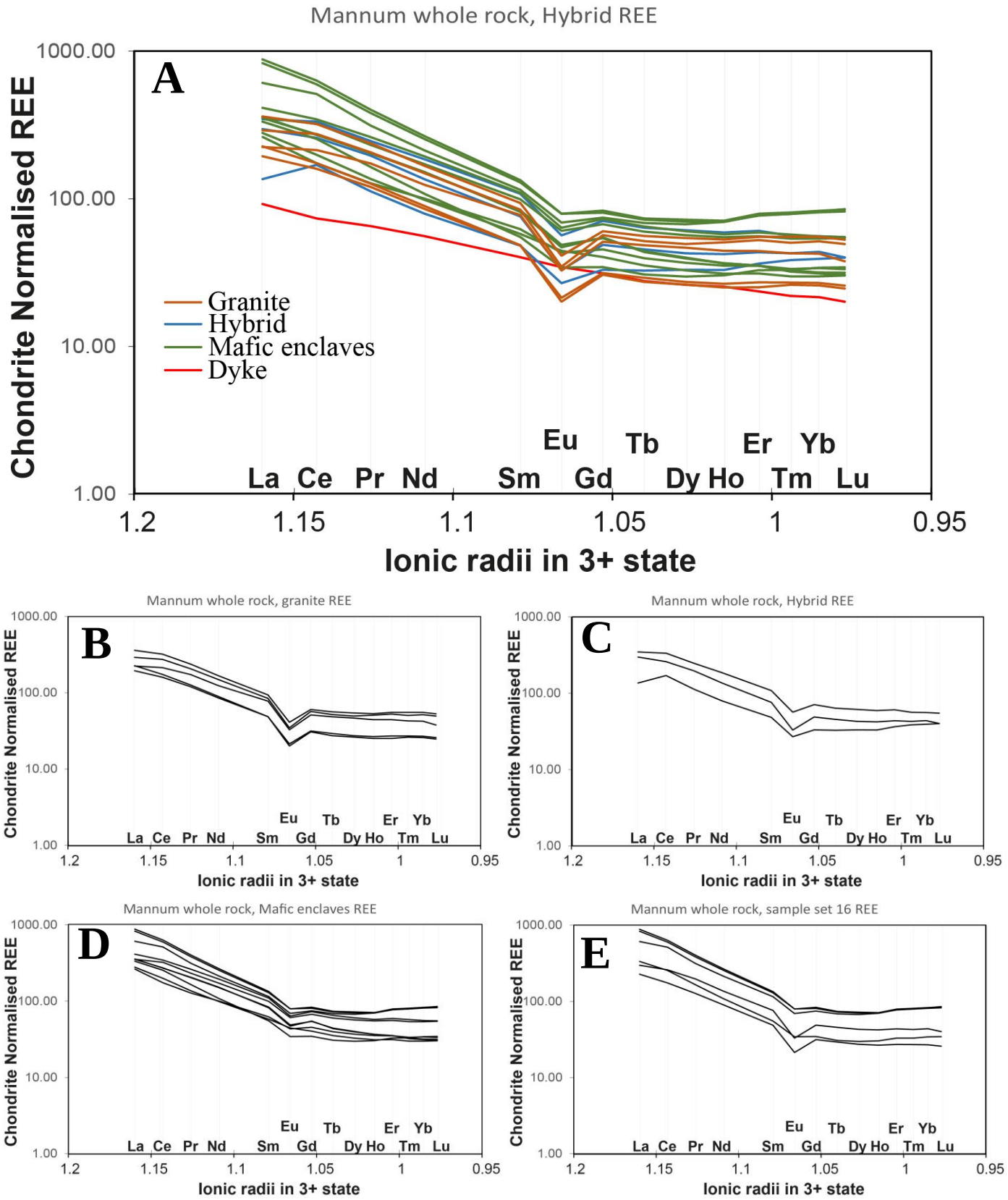

Figure 8: Whole rock rare earth element plots, normalised to CI carbonaceous chondrites. (A) all samples, MG7; the basalt dyke in red, hybrid samples in blue, mafic enclaves in green, granite in orange, (B) granite REE signatures, (C) hybrid REE signatures, (D) mafic enclave REE signatures, (E) sample set 16, ranging from granite, hybridised to mafic enclave REE signatures. Cl Chondrite values from Sun and McDonough (1996).

Individual mineral rare earth analysis

Individual mineral composition trace element analysis was done using LA-ICP-MS in samples: BOUNDARYts002, HYBRIDts006B, ENCLAVEts009 and BOUNDARYts012 for both sulphides and silicates. Titanite (Figure 9) and hornblende (Figure 10) were targeted due to a higher concentration of REEs compared to other silicates and their frequency in the enclaves, hybrid and granite phases (although hornblende is absent in granite). Feldspar and biotite were also targeted. But REE concentration, particularly of HREEs, were below detection limits for accurate analyses.

Titanite REE plots generally present similar trends apart from the Eu anomaly. Samples in mafic enclaves have a small positive or negative Eu anomaly (Figure 9A, B and C), while the titanites in BOUNDARYts016 and BOUNDARYts002 (Figure 9D and E) have a moderate negative Eu anomaly compared to the other REEs, which are all elevated in comparison to the mafic titanites.

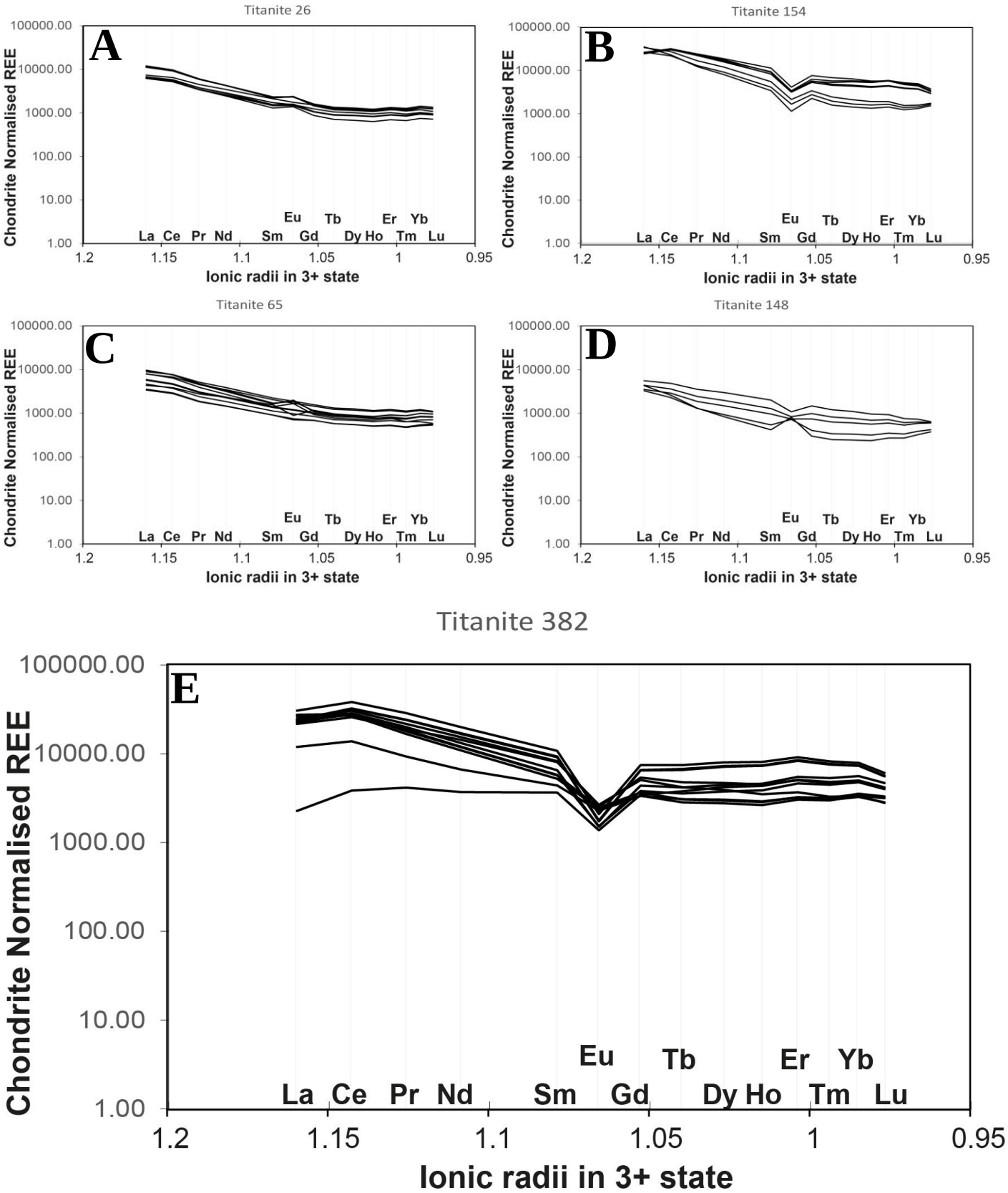

Figure 9: Titanite REE plots: (A) large titanite crystal in mafic enclave associated with a potassium feldspar crystal and a pyrite crystal, (B) large titanite in mafic enclave associated with a potassium feldspar crystal, (C) titanite crystal in mafic enclave associated with a potassium feldspar crystal, (D) subhedral titanite crystals in granite, near boundary with a mafic enclave, (E) euhedral titanite crystal in granite, near boundary with a mafic enclave. Cl Chondrite values from Sun and McDonough (1996).

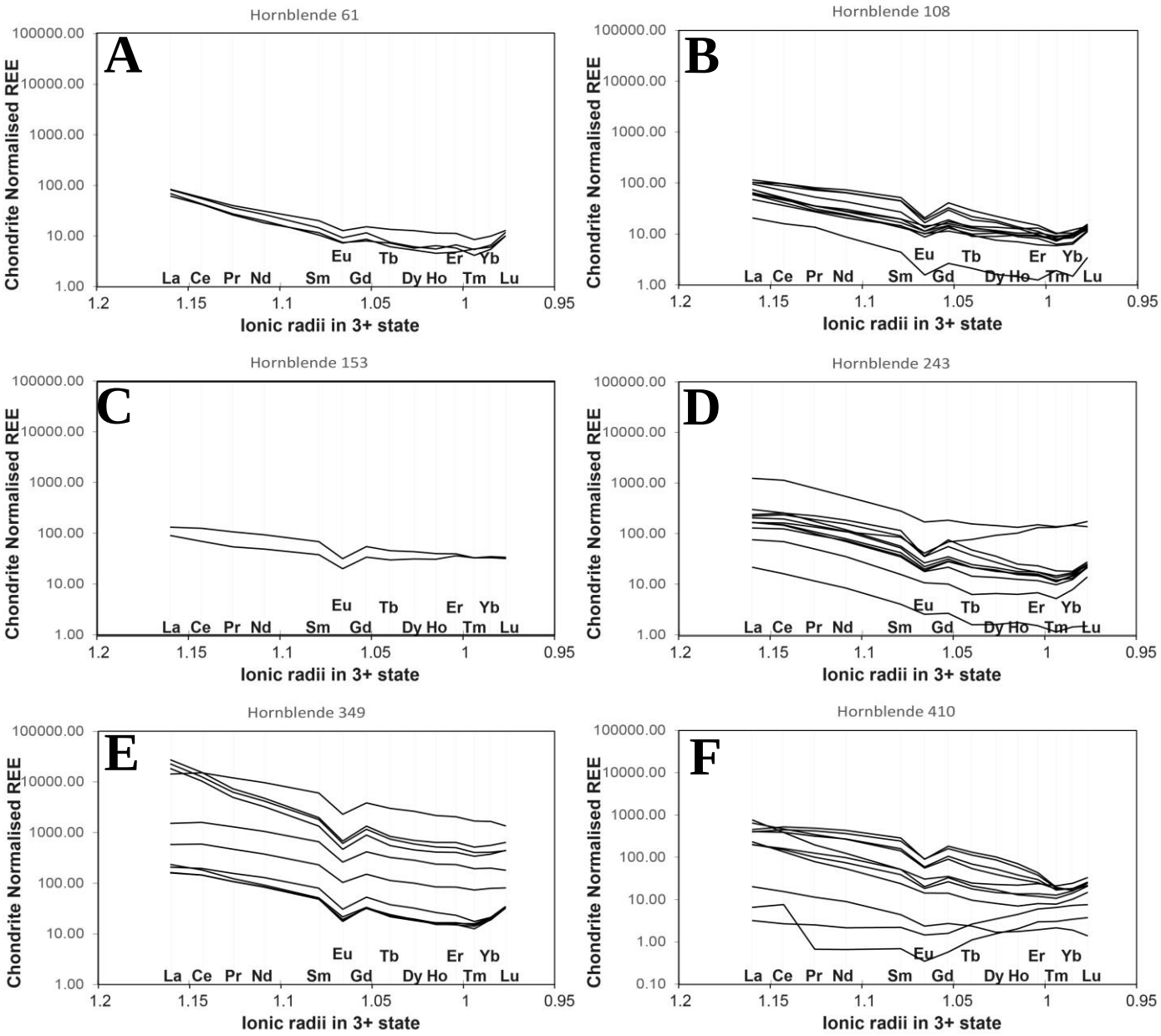

Figure 10: REE plots of hornblende crystals: (A, B, C) hornblende crystals in mafic enclaves, (D) hornblende crystal in mafic enclaves near boundary with granite, (E) hornblende crystals within mafic enclave, associated with a large anhedral mass of hornblende crystals, (F) hornblende crystal within mafic enclave near boundary with granite. Cl Chondrite values from Sun and McDonough (1996).

The REE signatures from hornblende crystals vary, displaying a wide range of REE concentrations with both positive and negative Eu anomalies. Hornblende crystals in ENCLAVEts009 (Figure 10A, B and C) follow a similar trend by having a small negative Eu anomaly. Hornblende crystals in BOUNDARYts002 (Figure 10D) are similar to those in BOUNDARY016 (Figure 10E and F) with hornblendes in BOUNDARYts016 being the most elevated in REEs

Copper concentration

Trace element concentrations of Cu and other transition metals together with sulphur are summarised in Table 9 and show that Cu is in low abundance (<40 ppm) in the Mannum granite samples, the dyke being slightly richer in Cu (50 ppm). Table 8 compares the correlation between transition metals and S or SiO_2.

Table 8: Shows R^2 values for select transition metals and SiO_2 and S, displaying the correlation between them.

	Cu	Co	Ni	Zn
SiO_2	0.647	0.223	0.489	0.387
S	0.818	0.73	0.357	0.433

Cu is most highly correlated with S, and somewhat correlated with SiO_2, while Co, Ni and Zn and are not strongly correlated with either S or SiO_2 (see Table 8). Understanding which minerals the targeted transition metals are concentrated in, enables transport processes to be better understood, and also provides information about possible isotope fractionation. The distribution of Cu appears to be linked with sulphur and this indicates that a volatile phase is transporting Cu, which may cause or drive isotope fractionation. Understanding the behaviour and quantity (Tables 9, 10 and 11) of other transition metals aids in Cu isotope analysis, as Zn and Ni can be used as spikes. However, if Cu purification is unsuccessful and Ni or Zn contaminate the sample, this causes the spike to be imprecise. Plots of Cu, Co, Ni and Zn against S and SiO_2 can be found in Appendix A.

Table 9: Solution ICP-MS analysis of trace elements in the Mannum granite rock suite. Targeted transition metals are shown.

Sample Name	S	Co	Ni	Cu	Zn
MG7	2506	57	85	50	123
HYBRID006B	856	17	5	13	127
HYBRID016B	259	20	2	4	64
HYBRID002A	2016	22	10	21	128
ENCLAVE016D	885	13	5	9	158
ENCLAVE 016E	1743	28	10	20	324
ENCLAVE 016F	1798	26	10	26	309
ENCLAVE 017A	2520	42	35	27	219
ENCLAVE 016C	1524	22	10	20	318
ENCLAVE 002B	2613	25	16	29	206
ENCLAVE 002C	2663	26	16	30	208
ENCLAVE 009B	1257	39	25	15	185
SD001A	867	29	7	14	130
SD001B	871	32	7	11	118
GRANITE012A	49	51	8	7	98
GRANITE 013A	287	17	2	4	60
GRANITE 016A	260	28	2	6	41
GRANITE 006A	322	25	3	4	72
GRANITE 012G	11	18	2	2	37

Measuring the amount of Cu in individual minerals aids in understanding the distribution and behaviour of Cu within the system. Table 10 displays a summary of targeted transition metals in rock forming minerals from LA-ICP-MS analysis and Table 11 summarises the values for pyrite. The data show that Co, Ni and Zn behave differently from Cu in their mineralogical distribution. This shows that Cu isotope analysis cannot necessarily be used to understand the behaviour of other transition metals. Note that Co is at elevated levels in pyrite but was not determined in the rock-forming minerals. EPMA data on sulphides are in Appendix B; the targeted transition metals were mostly below detection limits for EPMA.

Table 10: LA-ICP-MS data of targeted transition metals in rock-forming minerals, showing the average of analysis and the range of values. The number of analyses is displayed next to the mineral name.

Mineral/sample			
BOUNDARY002	**Ni**	**Cu**	**Zn**
Biotite (11)	29	12	930
	(1-66)	(0-56)	(58-1200)
Hornblende (19)	21	20	870
	(0-25)	(0-75)	(2-1300)
Matrix (16)	19	77	23
	(0-26)	(2-210)	(2-850)
HYBRID006B	**Ni**	**Cu**	**Zn**
	24	30	1100
Hornblende (15)	(3-61	(1-300)	(220-1500)
	13	2	450
Biotite (9)	(0-38	(1-6)	(14-1300)
ENCLAVE009	**Ni**	**Cu**	**Zn**
Biotite (25)	92	5	910
	(82-100)	(3-11)	(810-1200)
Hornblende (28)	59	1	680
	(0-120)	(0-6)	(3-820)
Matrix (15)	24	37	160
	(0-120)	(0-170)	(2-870)
BOUNDARY0016	**Ni**	**Cu**	**Zn**
Magnetite (20)	21	9	239
	(2-93)	(0-160)	(56-2000)
Biotite (12)	42	9	1300
	(31-48)	(2-37)	(1200-1600)
Matrix (17)	1	7	61
	(0-8)	(0-30)	(2-520)
Hornblende (43)	20	41	853
	(0-45)	(0-470)	(1-3200)

Table 11: LA-ICP-MS trace element data of transition metal concentrations in pyrite crystals averaged in different samples with minimum and maximum values.

sample	Co	Ni	Cu	Zn
BOUNDARYts002	1500	290	780	660
	(17-12000)	(16-1400)	(0-9700)	(1-27000)
HYBRIDts006C	740	350	5800	76
	(130-2400)	(75-1500)	(2-49000)	(3-370)
ENCLAVEts009	2700	2200	51	350
	(0-13000)	(15-33000)	(0-680)	(0-12000)
BOUNDARYts016	1300	240	260	370
	(9-7500	(17-1000)	(0-6500)	(1-5900)

Copper isotopes

Initial Cu isotope results were inconsistent and standards were approximately -1‰ out (Table 12) from literature values: USGS-BHVO-2 has an accepted value of $\delta^{65}Cu = 0.12$ (Moynier et al., 2017), USGS-GSP-2 has an accepted value of $\delta^{65}Cu = 0.30$ (Liu et al., 2014).

The Mannum granite samples initially showed a wide range of $\delta^{65}Cu$ values from 0.5‰ to -2.9.‰. In an attempt to overcome this problem, further analysis was conducted with samples prepared with hydrofluoric (HF) hotplate digestion. The results showed the standards were far closer to the expected $\delta^{65}Cu$ but still incorrect (Table 12), indicating HF bomb digestion caused fractionation, either through vaporisation and subsequent escape of a high ^{65}Cu vapor out of the bombs or possibly fractionation into fluorides which were undissolved and centrifuged out prior to Cu extraction.

The column ion exchange chromatography procedure was also modified to include two runs, the initial one, with a widened collection window, followed by a second run with the original collection volume; this was done to try and collect all the copper from the sample, then purify it, as impurities, such as Ti and Fe were suspected to alter the $\delta^{65}Cu$ value (Lowczak, 2019). However, this also produced inaccuracies in the standards USGS BHVO-2 and USGS GSP-2

(Table 12). Other metals such as Co, Ni and Zn were also of concern but this proved not to be an issue.

The molarity of HCl which carries samples through columns was investigated and was found to be in the range 5.81 to 5.7 Mol L^{-1}, while the copper column chromatography method calls for 6 Mol L^{-1} HCl. The molarity of the HCl controls the rate at which Cu cuts pass through the column. Maréchal and Albarède (2002) showed with 3 Mol L^{-1} HCl Cu cuts pass through after just 4 ml, while 7 Mol L^{-1} passes through after 20 ml; this drastic change in volume required to separate Cu indicates ^{65}Cu was being lost in the 7.5 ml eluting phase. Maréchal and Albarède (2002) also stated that a 90% collection may result in up to 0.3‰ change in the $\delta^{65}Cu$ value, which can greatly affect results. A Cu extraction was subsequently performed with 6 Mol L^{-1} HCl; only one run through the columns was performed on standard USGS BHVO-2, and a $\delta^{65}Cu$ value of 0.115‰ was achieved compared to the accepted value of 0.12. The other standard, GSP-2, returned a Ga uncorrected analysis of 0.312‰ compared to the accepted value of 0.3 (Moynier et al., 2017 and Liu et al., 2014). As both the BHVO-2 and GSP-2 only returned a single correct value the Cu isotope analysis is considered preliminary. The evolution of the Cu separation method used in this study, with reference to the $\delta^{65}Cu$ values for the standards, is summarised in Table 12.

Table 12: Cu isotope standard experiment results with date and change in method.

Date/change in method	BHVO-2 experimental $\delta^{65}Cu$ ‰	GSP-2 experimental $\delta^{65}Cu$‰
25/08/2021Original	**-0.942959**	**-0.947468**
13/09/2021 No bomb digestion	**-0.0727**	**0.1407**
25/09/2021Wider column collection	**-0.03**	**--**
11/10/2021 and 21/20/2021 Exact molarity of acid	**0.111**	**0.312**

After issues with Cu cuts collection had been solved, nine samples were analysed using MC-ICP-MS (Figure 11). The results for the analysed samples fit within the bounds of Rayleigh fractionation curves, showing that $\delta^{65}Cu$ is related to Cu concentration and becomes more

positive/heavier with decreasing Cu. Unfortunately, the analysis for two of the samples (HYBRID16B and ENCLAVE16D) was unsuccessful and a lack of time prevented repeat runs of these samples.

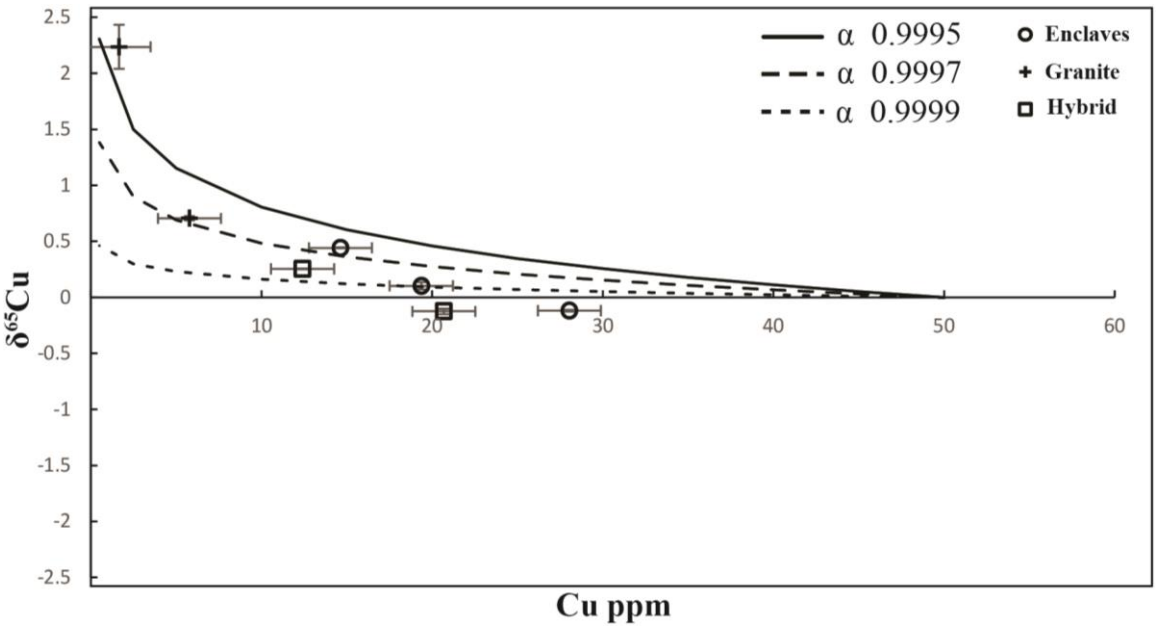

Figure 11: δ^{65}Cu data collected from Mannum granite with enclaves, granite and hybrid phases modelled against Cu concentration, with Rayleigh fractionation curves produced by Rayleigh fractionation factors α.

DISCUSSION

Whole rock textural evolution through mixing/mingling

Varying degrees of mingling and mixing between the mafic enclave and host granite were observed through petrographic analysis. The hybrid zones between the mafic enclaves and host granite vary in size and composition. Sample HYBRIDts006C is interpreted to be a completely mixed hybrid of the enclave and granite, as it possesses rapakivi feldspar, hornblende and plagioclase xenocrysts, and an increased frequency of pyrite and magnetite (Figure 5E). Samples GRANITEts006A and HYBRIDts6B (Figures 5C and 5D respectively) show incomplete mingling, as they lack any mafic minerals with the exception of rapakivi feldspars and minor pyrite. This is interpreted as a Na_2O rich melt/fluid interacting more reactively with the felsic crystal mush (Vernon, 2016). Sample BOUNDARYts001 shows a texturally abrupt granite-enclave boundary, showing no rapakivi texture mantling alkali feldspars (Figure 5A). The variation in the degree of mixing/mingling is possibly attributed to local thermal conditions; pressure is assumed to be constant across the system. Abrupt boundaries form as a result of a large difference in temperature between the granite and enclave, quenching the enclave as it is injected into the granite (Cherry and Trembath, 1978). In contrast the hybrid zones form as a result of the enclave and granite being closer in temperature during injection, preventing quenching. The degree of hybridisation is also associated with the proximity of mafic enclaves to microgranite blocks. Field observations show that the mafic enclaves and microgranite do not interact, with the enclaves deforming around the microgranite blocks. This is most likely due to the microgranite blocks being solid during the injection of the mafic enclaves (Turner and Foden, 1996). Turner and Foden (1996) reported a temperature of $\approx 930\,C^{o}$ after thermal equilibrium was achieved between the granite and the mafic enclaves, with mixing between the two phases likely occurring

before thermal equilibrium was reached. However, mingling may have continued after this point, allowing for more extensive formation of rapakivi feldspars. Several models have been proposed for the formation of rapakivi feldspars. The two main mechanisms proposed are: (1) isothermal decompression, where the feldspar stability field moves from alkali feldspar to plagioclase, and (2) a mechanism of mixing/mingling where mafic magma mingles into a crystal-rich felsic melt (Stewart, 1959; Hibbard, 1981; Calzia and Rämö, 2005). The rapakivi textures in the Mannum granite are strong textural evidence of the mixing/mingling of the magma of the mafic enclaves into the partially crystallized magma of the granite. Pankhurst et al. (2011) suggest multiple mixing events as opposed to mingling may have occurred due to the range in mafic enclave compositions reported by Turner and Foden (1996). Pankhurst et al. (2011) concluded that both the host granite and mafic enclaves had undergone fractional crystallisation and magma mingling/mixing. These two processes provide mechanisms for the transportation of material from a mafic source, such as the mantle, to the crust.

Whole rock geochemical evolution

The degree to which the host granite and mafic enclave phases have interacted, producing a third hybrid phase, was observed through whole rock major element analysis. Figure 12 shows the Harker plots calculated from the data from Figure 6 and Table 6, with added crystallisation vectors showing which minerals exert compositional control (Cortés, 2009). The trends presented in Figure 6 show a continuously evolving system, with two outliers: the mafic dyke, which is interpreted to be a later occurrence and distantly related to the Mannum granite and enclaves, and Sample ENCLAVEts017 which is the most mafic of the enclave samples. The trends visually resemble fractional crystallisation trends in Harker plots; however, they represent mixing/mingling trends in this case.

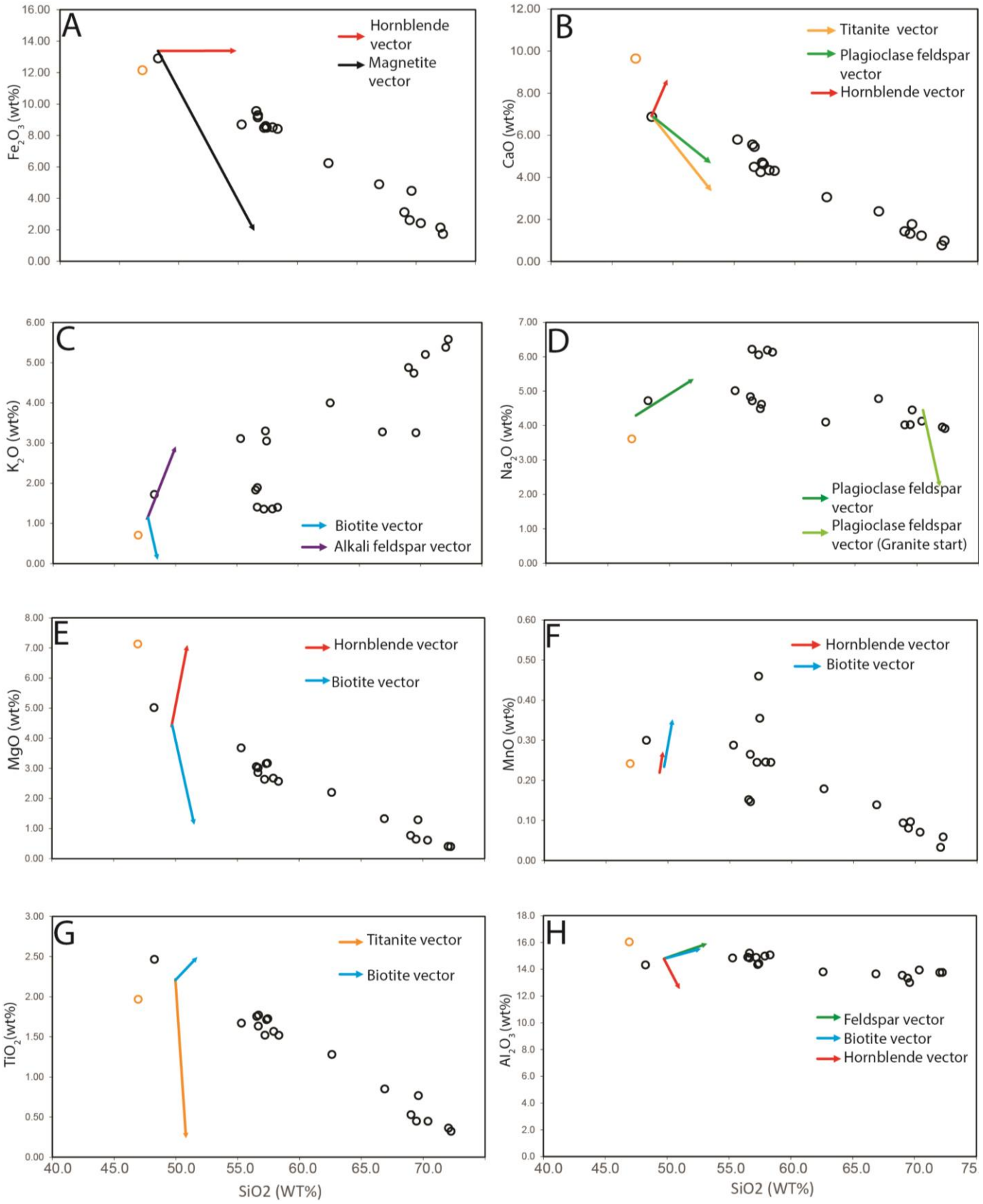

Figure 12: Crystallisation vectors on Harker plots from Figure 6 show the direction composition will take if mineralisation of a specific mineral occurs at 0%, 5%, 10% and 12%. Accessory minerals were modelled at 0% 2%, 4% and 6%, due to the low abundance of them within samples. The length of the vector shows the magnitude of whole rock composition change from the 0% mineralisation of a mineral to 12% mineralisation of a mineral and 6% in the case of accessory minerals.

The crystallisation vectors with Harker plots indicate which minerals control composition (Cortés, 2009; Harker, 1909). Fe_2O_3 is controlled by hornblende and magnetite, with magnetite exerting large control on Fe_2O_3 content; however, magnetite is present only as a trace phase (Figure 12A). Pyrite is also present, but in smaller quantities than magnetite. Fe_2O_3 is likely controlled by hornblende and to a smaller degree magnetite. The CaO content is predominantly controlled by plagioclase feldspar and hornblende. Titanite contains ≈ 28 (wt%) CaO, higher than the 9-12 (wt%) found in high Ca plagioclase feldspar and hornblende (Figure 12B); however, it is an accessory mineral making up at most only 1 -2% of the mineral assemblage in sample ENCLAVEts009. Na_2O is controlled by plagioclase feldspar; crystallisation vectors initially increase towards 57 wt% SiO_2, however Na_2O then decreases beyond this point as samples become more felsic (Figure 12D). K_2O is controlled by alkali feldspar and follows a fractional crystallisation trend (Figure 12C). MgO is controlled by both biotite and hornblende; these two minerals show vectors in opposing directions, however the MgO trend runs between them (Figure 12E). MnO is also controlled by biotite and hornblende and possibly small accessory minerals such as spinels (Figure 12F). TiO_2 is controlled by titanite and biotite, with the TiO_2 content of titanite ≈ 35-36.5 wt%, and is therefore mostly taken up into this mineral (Figure 12G). Al_2O_3 is taken up by biotite, feldspar and hornblende, however the amount of Al_2O_3 changes little in the overall system (Figure 12H). Whole rock chemistry analysis of Turner and Foden (1996) reported similar trends in Fe_2O_3, MnO, CaO and Na_2O vs SiO_2 plots, with the same MnO vertical trend at ≈57 wt% SiO_2; this vertical trend is possibly due to mineralisation of hornblende, and differences in individual enclave chemistries. The crystallisation vectors generally support the Harker plot trends. The Na_2O trend is relatively flat, decreasing only slightly from a central point of 57 wt% SiO_2, thus indicating that Na_2O is more mobile across the system, able to reside in the more felsic samples by forming rapakivi feldspars.

Whole rock rare earth elements

The whole rock REE plots show a negative Eu anomaly (Figure 8), as Eu^{2+} substitutes with Ca^{2+} in Ca-bearing minerals particularly plagioclase feldspar, thus indicating partial crystallisation of the original parental melt before injection of mafic melt into granite (Weill and Drake, 1973; Harrowfield et al., 1999). The low REE concentration of MG7, the Mannum dyke, indicates it originated from a different magma source. The mafic enclaves are slightly more enriched, overall, in REEs compared to the granite and hybrid material, and this may indicate a lack of REE transport or the presence of accessory minerals which can readily take in REEs, such as zircon.

Individual mineral chemical evolution

Hornblende REE patterns show a wide range of values following a general pattern of a small Eu anomaly, due to amphiboles taking up incompatible elements. The wide range of values most likely reflects the changing melt composition; as hornblende crystallises, it takes up incompatible elements. REEs being incorporated into hornblende may explain the higher enrichment of REEs in the mafic enclaves compared to the granite. The large hornblende crystal mass in BOUNDARYts016, shows elevated REEs indicating that it is a possible mafic xenocryst forming in a parental magma before injection.

Initial observations of titanites, in ENCLAVEts009 particularly, indicated that they are xenocrysts due to their association with alkali feldspar. The two minerals possess a euhedral edge with each other while having anhedral edges with the rest of the assemblage; this is interpreted as the titanite and alkali feldspar being xenocrysts from the granite and being assimilated and partially remelted resulting in the external anhedral edge (Figure 5F). Pyrite is also often associated with these titanite-alkali feldspar crystals, indicating a later stage fluid interaction or that these crystals have originated in an immiscible melt. These titanite-alkali

feldspar-pyrite crystals are exclusive to sample ENCLAVEts009 indicating there may have been unique mixing/mingling conditions and behaviours within individual mafic enclaves. REE analysis of the titanites however, reveals that they most likely formed in a mafic environment, as discussed by Pankhurst et al. (2011). REEs are overall depleted in mafic titanites (ENCLAVEts009) compared to felsic titanites (titanites within BOUNDARYts002 and BOUNDARYts016), while mafic titanites display a lesser Eu anomaly (Figure 9A, B and C). REE data indicate that titanites have grown within the mafic enclaves, and are not xenocrysts. However, the euhedral edge association with large alkali feldspars provides evidence towards an assimilation of xenocrysts from the host granite during injection of the mafic enclaves. This possibly indicates that the alkali feldspar xenocrysts are a result of a felsic immiscible melt and that felsic material mingles with the mafic enclaves more readily than the mafic material in the granite, which is restricted to near the enclave-granite boundary or in hybrid zones (Kamenetsky and Kamenetsky, 2010). However, this does not explain the observed relationship with large titanites and pyrite.

LA-ICP-MS analysis also showed the quantity of Cu in individual minerals (see Tables 9, 10 and 11) and that Cu concentration in the individual minerals are generally low, <100 ppm, but there is considerable variation. For example, the pyrite in the ENCLAVEts009 sample carries significantly less Cu than pyrites in other samples; however, the pyrite crystals in this sample may be a late-stage product as these often larger crystals are in association with titanite-alkali feldspar and are anhedral, indicating a product of magmatic fluids (Figure 5F) (Polyakov and Soultanov, 2011). Pyrite in sample HYBRIDts006B has a much higher Cu content (mean of 5800 ppm) compared to other samples (mean of <1000 ppm), indicating that Cu was transported during hybridisation. Cu was shown in Table 8 to correlate with S; the formation of sulphides can lead to a large degree of Cu isotope fractionation (Brzozowski

et al., 2020). Note that Co concentration was determined, as Co is not separated from Cu through column ion exchange chromatography, and may cause interference in MC-ICP-MS at high enough concentrations (>1000 ppb) (Kidder et al., 2020). Ni and Zn were measured as they can be used for internal standard spikes for MC-ICP-MS and will affect the δ^{65}Cu value if not removed through ion exchange chromatography (this was not an issue in this study as Ga was used as an internal standard). In the current study Cu isotope analysis was used to determine if this Cu was fractionated during the formation of pyrites.

Copper isotope behaviour

Preliminary Cu isotope analysis results show that Cu isotope ratios in the Mannum granite-mafic enclave system follow a Rayleigh fractionation distribution (Figure 11). Figure 11 shows that δ^{65}Cu increases with decreasing Cu concentration. As the Mannum granite is a high energy setting, ≈ 930 C^{o}, after thermal equilibrium (Turner and Foden, 1996), very little isotopic fractionation occurred, with the more mafic samples with higher Cu becoming more isotopically lighter (negative δ^{65}Cu). ^{65}Cu has a slight preference for remaining in the melt. Sample ENCLAVE009 shows a slight elevation compared to other enclave samples and even hybrid samples; this may be due to the apparent magmatic fluid movement (Figure 5F). In ENCLAVE009, the ^{65}Cu values still lie within Rayleigh fractionation curves, the higher ^{65}Cu values also showing that the amount of Cu and S measured is accurate. Figure 11 shows that Cu is being transported to some extent from the mafic enclaves to the granite and hybrid phases following the Rayleigh fractionation trend. This indicates that Cu is preferentially remaining in the mafic enclaves, but a small quantity is being transported with the mafic material during mixing/mingling with the granite.

The issues experienced with Cu isotope analysis in this project highlight the importance of the use of high-quality isotopic reference standards. A variety of issues involving sample digestion and separation through ion exchange chromatography were identified through measuring of these isotope standards. The use of bomb digestion was found probably to cause significant Cu fractionation. Bomb digestion was originally used, as certain minerals in the granite such as zircon are very difficult to digest. However, it is not necessary for Cu isotope analysis. The molarity of the HCl proved to be a critical factor in the full separation and collection of Cu. Maréchal and Albarède (2002) stated that 90% collection may result in up to 0.3‰, with a small change in the molarity of HCl leading to incomplete collection. The reason the molarity of HCl is critical is due to the coordination chemistry of copper-aqua-chloro complexes. Brugger et al. (2001) showed at 25°C that the nature of the Cu^{2+} changes considerably with the concentration of the Cl^- ion, at 2 Mol L^{-1} Cl^- $(Cu(H_2O)_6)^{2+}$ is the dominant complex, at 4 Mol L^{-1} Cl^- a mixture of $(Cu(H_2O)_6)^{2+}$, $(Cu^{2+}Cl(H_2O)_5)^+$ and $(Cu^{2+}Cl_2(H_2O)_4)$ occur in roughly equal abundance, and between 6 Mol L^{-1} and 8 Mol L^{-1} the $(Cu^{2+}Cl_2(H_2O)_4)$ complex is most abundant and stable. This complex is a Jahn-Teller distorted octahedral complex with the two Cl ions occupying opposite apical sites (Brugger et al., 2001; Halcrow, 2013). The Cl concentration is critical to the stabilisation of the complex, as at lower concentrations of Cl the complex will move to mixtures of the $(Cu(H_2O)_6)^{2+}$ and $(Cu^{2+}Cl(H_2O)_5$ complexes. This is because H_2O molecules are stronger ligands than Cl ions (Halcrow, 2013). The stability of polar Cu^{2+} complexes enables Cu to be separated out from the other metals in an ion exchange column between the intervals of 7.5 ml to 25.5 ml of 6 Mol L^{-1} HCl (Maréchal and Albarède, 2002). This understanding of Cu complex coordination chemistry can be related to Cl-rich hydrothermal fluids, Cl-rich fluids being able to transport Cu more readily; this may also have an isotopic effect with $^{65}Cu^{2+}Cl_2(H_2O)_4$ being very slightly more stable and less likely to exchange ligands than $^{63}Cu^{2+}Cl_2(H_2O)_4$. In high

temperature and highly saline hydrothermal fluids (greater than 250°C and >10 Mol L^{-1} Cl^{-}, Cu is transported as a $CuCl_4$ tetrahedral complex (Brugger et al., 2001; Liu et al., 2002). This means ^{65}Cu is preferentially more mobile, leading to the initial few ml of Cu cuts from the ion exchange separation column being enriched in ^{65}Cu. This effect of greater ^{65}Cu mobility is reflected in the measured Cu isotopes results, with ^{65}Cu being slightly more concentrated in the granite, which Cu is transported into. Due to the preliminary nature of the Cu isotope analysis presented in this study, a number scenarios surrounding the Cu isotopic ratios of the Mannum granite have been constructed to show the possible variations in $\delta^{65}Cu$ and the implications these data would have (Figure 13).

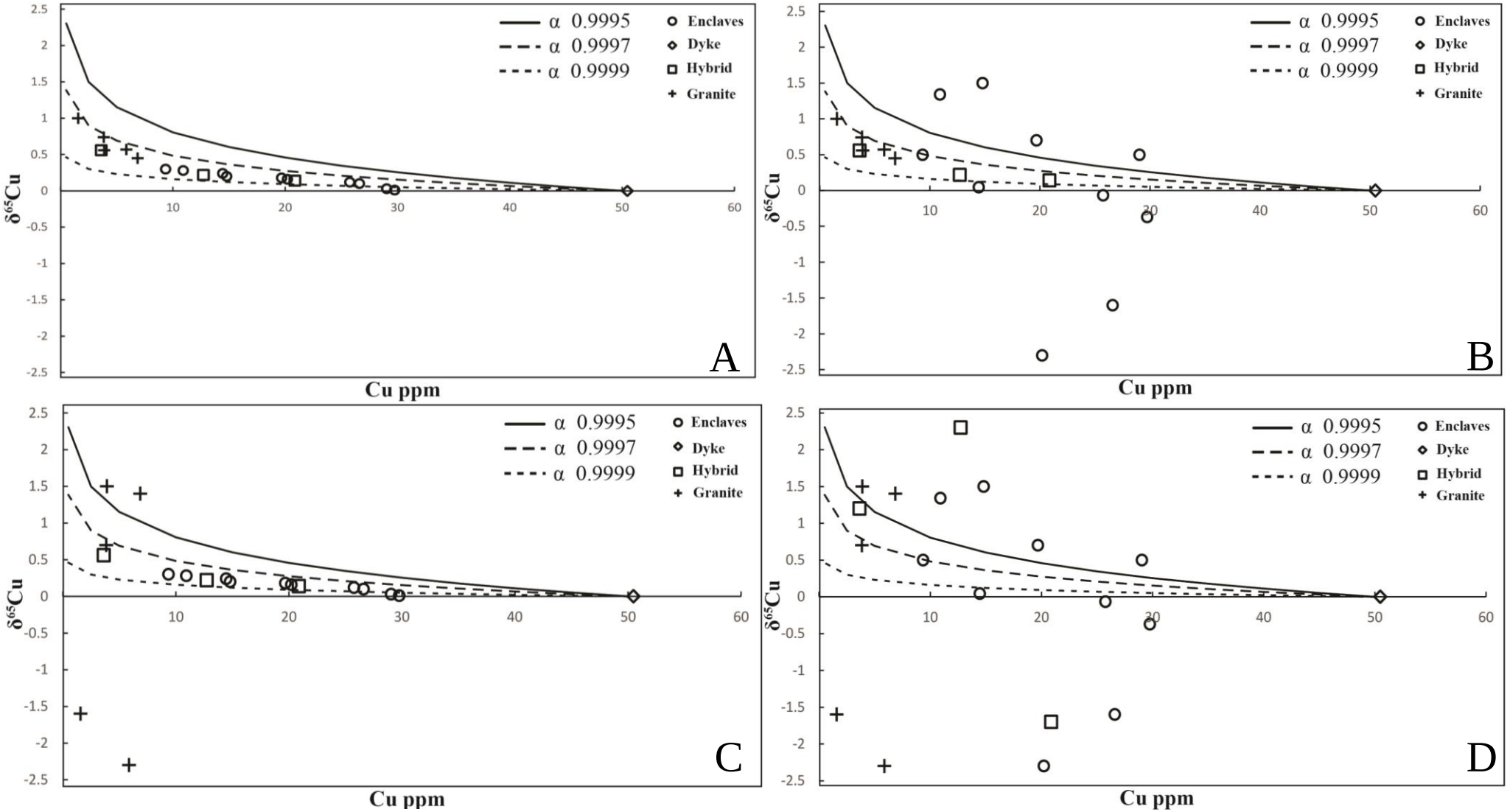

Figure 13: Cu isotope schematics with possible results of Cu isotope analysis modelled with copper concentration in each of the samples. Compositional phases are divided and Rayleigh fractionation curves show the range of isotope fractionations through Rayleigh fractionation factors α. (A) Cu isotope fractionation follows Rayleigh fractionation curve. (B) Mafic enclave samples display a large range of δ^{65}Cu. (C) Granite samples display a large range of δ^{65}Cu. (D) All samples display a large range of δ^{65}Cu.

If Cu isotope data were successfully collected, δ^{65}Cu values may have displayed differences in copper chemistry. Figure 13A shows δ^{65}Cu values controlled by Rayleigh fractionation; very little Cu fractionation has occurred (Mathur et al., 2012), reflecting the preliminary results presented in this study. Figure 13A displays narrow mantle values between -0.15 to 0.18‰ in the enclave samples and up to1‰ in the granite (Liu et al., 2015). The granitic samples, with low Cu content, display a higher δ^{65}Cu due to the relationship between decreasing Cu concentration and increasing δ^{65}Cu (Mathur et al., 2012).

Figure 13B shows a high degree of variation of δ^{65}Cu in mafic enclave samples; this would indicate that the mafic enclaves have undergone a highly fractionating process, such as metasomatism or interaction with magmatic fluids. The granite samples show low variation in δ^{65}Cu, showing that Cu has not been transferred to the granite from the mafic enclaves to any large degree; the hybridised samples show no variation in δ^{65}Cu. In this scenario there has been minimal transfer of Cu between the two phases, or the highly fractionated nature of the Cu in mafic enclaves is a later occurrence. The drastic difference in δ^{65}Cu may also suggest a different origin for the two magmas (Larson et al., 2003).

Figure 13C shows a high degree of variation of δ^{65}Cu in granite samples, showing the copper within the host granite to be highly fractionated, possibly from metasomatism, assimilation of country rock, or interaction with magmatic fluids. The mafic enclaves, however, originate from a less fractionated source, with respect to Cu, or have not been exposed to any processes which would lead to a large degree of Cu isotope fractionation (Larson et al., 2003).

In Figure 13D both the granite and mafic enclaves are highly fractionated. This indicates that the parental magma of both enclaves and granite is a highly fractionated source, or that a process or multiple processes have caused a large variation in δ^{65}Cu, such as metasomatism, assimilation of a highly fractionated Cu source, or interaction with magmatic fluids. Alternatively, either the granite or enclaves may possess the large variation of δ^{65}Cu, such as

in Figures 13B and 13C, and the Cu has been transferred between the two phases, resulting in overall change of δ^{65}Cu (Liu et al., 2014).

Clearly, due to the preliminary nature of the δ^{65}Cu fractionation results, a number of replicate analyses need to be undertaken before more definite conclusions can be reached on the mechanism of Cu fractionation in this system.

CONCLUSIONS

The Mannum granite provides insight into the transfer of material between two magmatic phases of different composition and gives insight into the behaviour of Cu isotopes in an evolving magmatic system. Whole rock and mineral major and trace element analysis and Cu isotope analysis support the following conclusions:

1. Magma mingling and to a smaller extent mixing show the transfer of plagioclase feldspar into the granite phase leading to the formation of rapakivi feldspars. They also show the transfer of xenocrysts of minerals such as hornblende, alkali feldspar, pyrite and plagioclase, between the two phases, concentrating in a third hybrid phase.
2. The origins of the titanite-alkali feldspar-pyrite associations are unresolved. The euhedral relationship between the titanite and alkali feldspar indicates that they grew together, while titanite REE signatures, small Eu anomaly and lower overall REEs compared to titanites in the granite, indicate that titanites have grown in the mafic enclaves. Both titanite and alkali feldspar display anhedral edges with the surrounding mafic enclave, possibly from reabsorption into the mafic melt. Alternatively, titanite and alkali feldspar resulted from immiscible melt inclusions, hence the euhedral internal and anhedral external edges. The association with pyrite may indicate fluid mobility or a high Fe and S content of the immiscible fluid.

3. Preliminary Cu isotope analysis showed that $\delta^{65}Cu$ positive increase is correlated to decreasing Cu concentration. $\delta^{65}Cu$ values follow a Rayleigh fractionation curve as the heavier isotope remains in the magma slightly more readily than the light isotope. The small range of ^{65}Cu values in the enclaves and hybrid samples measured shows an apparent lack of fluid mobility.

FUTURE WORK

Drill core samples or fresh samples from within the Mannum granite, in contrast with the exposed outcrop sequences used in this study, would likely provide more certainty to whole rock chemistry and possibly allow for the full extent of the mafic enclaves within the granite to be explored. Cu, Fe and Zn isotopes could be used to compare the role of hydrothermal fluids and magmatism in metal transport, as Redox sensitivity and petrogenesis can be better constrained (Fernandez and Borrok, 2009; Foden et al., 2015). Thermometry and more extensive REE analysis may show the origin of the alkali feldspar-titanite-pyrite associations. Though the alkali feldspar is clearly a xenocryst either from an immiscible melt or from the granite phase, the titanites, as evidenced by REE signatures, are native to the mafic enclaves. Thermometry will show the temperature at which large titanites formed relative to the surrounding mafic enclaves. Extensive analysis of titanites within all phases may well aid in discriminating titanite growth generations. REE analysis of titanites within the mafic enclaves which are not associated with alkali feldspar or pyrite may indicate if there are multiple generations of titanite growth and may provide information on the origin of titanites in the mafic enclaves. SEM imaging of titanites may show zoning; McLeod et al. (2010) showed that zoning in titanite is related to mixing/mingling. Further investigation into the formation

of Cu complexes, and how Cu isotopes fractionate in response, in magmatic rocks would aid in the understanding of the role of mafic magmas in Cu transport.

ACKNOWLEDGMENTS

I would like to thank my supervisors Lucy McGee and Justin Payne for their continuous support, guidance and patience throughout the year, particularly during the Cu isotope period of this project. I am grateful to MinEx CRC for the financial support and to John Foden for his knowledge on the Mannum granite and transition metal isotopes, and for his support during the year. The staff at Adelaide Microscopy, Sarah Gilbert, Aoife McFadden and Benjamin Wade, have been a huge source of assistance. Big thanks to Robert Klaebe for continuous help and inductions, along with Bradly Cave and Zara Woolston for their help in the clean laboratory. Thanks to Claire Wright at the CSIRO Waite campus for help with Cu isotope analysis. Derrick Hasterok and Katie Howard are acknowledged for all the effort and time that they have put into coordinating Honours this year. Thanks to all the other Honours students for mutual support. Thank you to my parents for help with proofreading.

REFERENCES (LEVEL 1 HEADING)

BARNES, C. G., WERTS, K., MEMETI, V., PATERSON, S. R., BREMER, R., (2021), A tale of five enclaves: Mineral perspectives on origins of mafic enclaves in the Tuolumne Intrusive Complex, *Geosphere*, 17, 352–374.

BEA, F., PEREIRA, M. D., STROH, A. S., (1994), Mineral/leucosome trace-element partitioning in a peraluminous migmatite (a laser ablation-ICP-MS study), *Chemical Geology*, 117, 291-312.

BIGELEISEN, J., MAYER, M. G., (1947), Calculation of Equilibrium Constants for Isotopic Exchange Reactions, *Journal of Chemical Physics*, 15, 261-267.

BRUGGER, J., MCPHAIL, D. C., BLACK, J., SPICCIA, L., (2001), Complexation of metal ions in brines: application of electronic spectroscopy in the study of the Cu(II)-LiCl-H2O system between 25 and 90°C, *Geochemica et Cosmochimica Acta*, 65, 2691-2708.

BRZOZOWSKI, M. J., GOOD, D. J., WU, C., LI, W., (2020), Cu isotope systematics of conduit-type Cu–PGE mineralization in the Eastern Gabbro, Coldwell Complex, Canada, *Mineralium Deposita*, 56, 707–724.

CALZIA, J. P., RÄMÖ, O. T., (2005), Miocene rapakivi granites in the southern Death Valley region, California, USA. *Earth Science Reviews*, 73, 221–243.

CHERRY, M. E., TREMBATH, L. T., (1978), The pressure quench formation of rapakivi texture, *Contributions to Mineralogy and Petrology*, 68, 1–6.

CORTÉS, A. J., (2009), On the Harker Variation; A Comment on "The Statistical Analysis of Compositional Data. Where Are We and Where Should We Be Heading?" by Aitchison and Egozcue (2005), *Mathematical Geosciences*, 41, 817-828.

COX, D., WATT, S. F. L., JENNER, F. E., HASTIE, A. R., HAMMOND, S. J., KUNZ, B., (2020), Elevated magma fluxes deliver high-Cu magmas to the upper crust, Geology, 48, 957-960.

DEPAOLO, D. J., (1981), Trace element and isotopic effects of combined wallrock assimilation and fractional crystallization, *Earth and Planetary Science Letters*, 53, 189-202.

FROST, B. R., BARNES, C. G., COLLINS, W. J., ARCULUS, R. J., ELLIES, D. J., FROST, C. D., (2001), A Geochemical Classification for Granitic Rocks, *Journal of Petrology*, 42, 2033-2048.

FERNANDEZ, A., BORROK, D. M., (2009), Fractionation of Cu, Fe, and Zn isotopes during the oxidative weathering of sulfide-rich rocks, *Chemical Geology*, 264, 1-12.

FODEN, J., ELBURG, M. A., DOUGHERTY-PAGE, J., BURTT, A., (2006), The timing and duration of the Delamerian Orogeny: Correlation with the Ross Orogen and implications for Gondwana Assembly, *The Journal of Geology*, 114, 189-210.

FODEN, J., ELBURG, M., TURNER, S., CLARK, C., BLADES, M. L., COX, G., COLLINS, A. S., WOLFF, K., GEORGE, C., (2020), Cambro-Ordovician magmatism in the Delamerian orogeny: Implications for tectonic development of the southern Gondwanan margin, *Gondwana Research*, 81, 490-521.

FODEN, J. D., ELBURG, M. A., TURNER, S. P., SANDIFORD, M., O'CALLAGHAN, J., MITCHELL, S., (2002), Granite production in the Delamerian Orogen, South Australia, *Journal of the Geological Society*, 159, 557-575.

FODEN, J., SOSSI, P. A., WAWRYK, C. M., (2015), Fe isotopes and the contrasting petrogenesis of A-, I- and S-type granite, *Lithos*, 212, 32-44.

FODEN, J., SONG, S. H., TURNER, S., ELBURG, M., SMITH, P. B., DER STELDT, B. V., PENGLIS, D. V., (2002), Geochemical evolution of lithospheric mantle beneath S.E. South Australia, *Chemical Geology*, 182, 663-695.

GIBSON, G. M., CHAMPION, D. C., IRELAND, T. R., (2015), Preservation of a fragmented late Neoproterozoic–earliest Cambrian hyper-extended continental-margin sequence in the Australian Delamerian Orogen, *Geological Society, London, Special Publications*, 413, 269-299.

HALCROW, M. A., (2013), Jahn–Teller distortions in transition metal compounds, and their importance in functional molecular and inorganic materials, *Royal Society of Chemistry*, 42, 1784-1795.

HARKER, A., (1909), *The Natural History of Igneous Rocks*, Cambridge University Press.

HARROWFIELD. J. M, OGDEN, M. I., RICHMOND, W. R., WHITE, A. H., (1999), Lanthanide ions as calcium substitutes: a structural comparison of europium and calcium complexes of a ditopic calixarene, *J. Chem. Soc., Dalton Trans*., 1991, 2153-2160.

HIBBARD, M. J., (1981), The magma mixing origin of mantled feldspars. *Contributions to Mineralogy and Petrology* 76, 158–170.

HOGAN, J. P., GILBERT, M. C., PRICE, J. D., (2000), Crystallisation of fine- and coarse-grained A-type granite sheets of the Southern Oklahoma Aulacogen, U.S.A. *Transactions of the Royal Society of Edinburgh Earth Sciences*, 91, 139–150.

HUANG, J., LIU, S., GAO, Y., XIAO, Y., CHEN, SHA., (2016), Copper and zinc isotope systematics of altered oceanic crust at IODP Site 1256 in the eastern equatorial Pacific, *Journal of Geophysical Research: Solid Earth*, 121, 7086-7100.

KAMENETSKY. V. S., KAMENETSKY. M. B., (2010), Magmatic fluids immiscible with silicate melts: example from inclusions in phenocrysts and glasses, and implications for magma evolution and melt transport, *Geofluids*, 10, 293-311.

KENDALL, C,, CALDWELL, E. A,, (1998), Fundamentals of Isotope Geochemistry, In KENDALL, C, and MCDONNELL J. J. (eds), *Isotope Tracers in Catchment Hydrology*, Elsevier Science.

KIDDER, J. A., VOINOT, A., SULIVAN, K. V., CHIPLEY, D., VALENTINO, M., LAYTON-MATTHEWS, D, L. EYBOURNE, M., (2020), Improved ion-exchange column chromatography for Cu purification from high-Na matrices and isotopic analysis by MC-ICPMS, *Journal of Analytical Atomic Spectrometry*, 35, 776-783.

LARSON, P. B., MAHER, K., RAMOS, F. C., CHANG, Z., GASPAR, M., MEINERT, L. D., (2003), Copper isotope ratios in magmatic and hydrothermal ore-forming environments, *Chemical Geology*, 201, 337-350.

LIU, W., BRUGGER, J., MCPHAIL, D. C., SPICCIA, L., (2002), A spectrophotometric study of aqueous copper(I)–chloride complexes in LiCl solutions between 100 °C and 250 °C, *Geochimica et Cosmochimica Acta*, 66, 3615-2633.

LIU, S., HUANG, J., LIU, J., WÖRNER, G., YANG, W., TANG, Y., CHEN, Y., TANG, L., ZHENG, J., LI, S., (2015), Copper isotopic composition of the silicate Earth, *Earth and Planetary Science Letters*, 427, 95-103.

LIU, S., LI, D., LI, S., TENG, F., KE, S., HE, Y., LU, Y., (2014), High-precision copper and iron isotope analysis of igneous rock standards by MC-ICP-MS, *Journal of Analytical Atomic Spectrometry*, 29, 122-133.

LIU, S., LI, Y., LIU, J., YANG, Z., LIU, J., SHI, Y., (2021), Equilibrium Cu isotope fractionation in copper minerals: a first-principles study, *Chemical Geology*, 564, 120060.

LOWCZAK, C. R., (2019), *Copper isotope method development for determining the source of mineralised provinces*, Honours thesis, The University of Adelaide.

LV, N., BAO, Z., CHEN, L., CHEN, K., ZHANG, Y., YUAN, H., (2020), Accurate determination of Cu isotope compositions in Cu-bearing minerals using microdrilling and MC-ICP-MS, *International Journal of Mass Spectrometry*, 457, 116414.

MARÉCHAL, C., ALBARÈDE, F., (2002), Ion-exchange fractionation of copper and zinc isotopes, *Geochimica et Cosmochimica Acta*, 66, 1499-1509.
MARÉCHAL, C. N., TÉLOUK, P., ALBARÈDE, F., (1999), Precise analysis of copper and zinc isotopic compositions by plasma-source mass spectrometry, *chemical geology*, 156, 251-273.
MATHUR, R., JIN, L., PRUSH, V., PAUL, J., EBERSOLE, C., FORNADEL, A., WILLIAMS, J. Z., BRANTLEY, S., (2012), Cu isotopes and concentrations during weathering of black shale of the Marcellus Formation, Huntingdon County, Pennsylvania (USA), *Chemical Geology*, 305, 175-184.
MCDONOUGH, W. F., SUN, S., (1995), The composition of the Earth, *Chemical Geology*, 120, 223-253.
MILLER, J. MCL., PHILLIPS, D., WILSON, C. J. L., DUGDALE, L. J. (2005), Evolution of a reworked orogenic zone: The boundary between the delamerian and lachlan fold belts, southeastern Australia, *Australian Journal of Earth Sciences*, 52, 6, 921-940.
MOYNIER, F, VANCE, D, FUJI, T, Savage, P., (2017), The Isotope Geochemistry of Zinc and Copper, *Reviews in mineralogy and Geochemistry*, 82, 543-600.
NEKVASIL, H., (1991), Ascent of felsic magmas and formation of rapakivi. *American Mineralogist* 76, 1279–1290.
PANKHURST, M. J., VERNON, R. H., TURNER, S. P., SCHAEFER, B. F., FODEN, J. D., (2011), Contrasting Sr and Nd isotopic behaviour during magma mingling; new insights from the Mannum A-type granite, *Lithos*, 126, 135-146.
PLAIL, M., BARCLAY, J., HUMPHREYS, M. C. S., EDMONDS, M., HERD, R. A., CHRISTOPHER, T. E., (2014), Chapter 18 Characterization of mafic enclaves in the erupted products of Soufrière Hills Volcano, Montserrat, 2009 to 2010, *Geological Society, London, Memoirs*, 39, 343-360.
POLYAKOV, V. B., SOULTANOV, D. M,, (2011) New data on equilibrium iron isotope fractionation among sulfides: Constraints on mechanisms of sulfide formation in hydrothermal and igneous systems, *Geochimica et Cosmochimica Acta*, 75, 1957-1974
RAYMOND, L. A., (1943), Petrology: the study of igneous, sedimentary, metamorphic rocks. Dubuque, Iowa : Wm. C. Brown
SHIELDS, W. R., MURPHY, T. J., GARNER, E. L., (1964), Absolute isotopic abundance ratio and the atomic weight of a reference sample of copper, *Journal of Research of the National Bureau of Standards Section A: Physics and Chemistry*, 68A, 6, 589.
STEWART, D.B., 1959. Rapakivi granite from eastern Penobscot Bay, Maine. *20th International Geological Congress, Mexico*, pp. 293–320.
SUN, W, WANG, J, ZHANG, L, ZANG, C, LI H, LING, M, DING, X, LI, C, LIANG, H, (2017), The formation of porphyry copper deposits, *Acta Geochim*, 36, , 9-15.
TURNER, S. P., (1996), Petrogenesis of the late-Delamerian gabbroic complex at Black Hill, South Australia: implications for convective thinning of the lithospheric mantle. *Mineralogy and Petrology* , 56, 51-98.
TURNER, S. P., and FODEN, J., (1996), Magma mingling in late-Delamerian A-type granites at Mannum, South Australia, *Mineralogy and Petrology*, 56, 147-169.
TURNER, S. P., FODEN, J. D., MORRISON, R. S., (1992), Derivation of some A-type magmas by fractionation of basaltic magma: An example from the Padthaway Ridge, South Australia, *Lithos*, 28, 151-179.
UREY, H. C., (1947), The thermodynamic properties of isotopic substances, *Journal of the Chemical Society*, 562.
VERNON, R. H. (2016), Rapakivi granite problems: plagioclase mantles and ovoid megacrysts, *Australian Journal of Earth Sciences*, 63, 675-700.
WARK, D.A., STIMAC, J.A., (1991). Origin of mantled (rapakivi) feldspars; experimental evidence of control by a dissolution- and diffusion-controlled mechanism. Eos, Transactions, American Geophysical Union 72, 304.
WEILL, D.F, DRAKE, M. J, (1973), Europium Anomaly in Plagioclase Feldspar: Experimental results and Semiquantitative model, *Science*, 180, 4090, 1059-1060.
WU, F., LIU, X., JI, W., WANG, J., YANG, L. (2017), Highly fractionated granites: Recognition and research, *Science China Earth Sciences*, 60, 7, 1201-1219.
YAXLEY, G. M. (2000), Experimental study of the phase and melting relations of homogeneous basalt mathplus peridotite mixtures and implications for the petrogenesis of flood basalts, *Contributions to Mineralogy and Petrology*, 139, 3, 326-338.
ZHENG, Y., LIU, S., WU, C., GRIFFIN, W, L., LI, Z., XU, B., YANG, Z., HOU, Z., O'REILLY, S, Y., (2018),Cu isotopes reveal initial Cu enrichment in sources of giant porphyry deposits in a collisional setting, geology, 47, 135-138

APPENDIX A

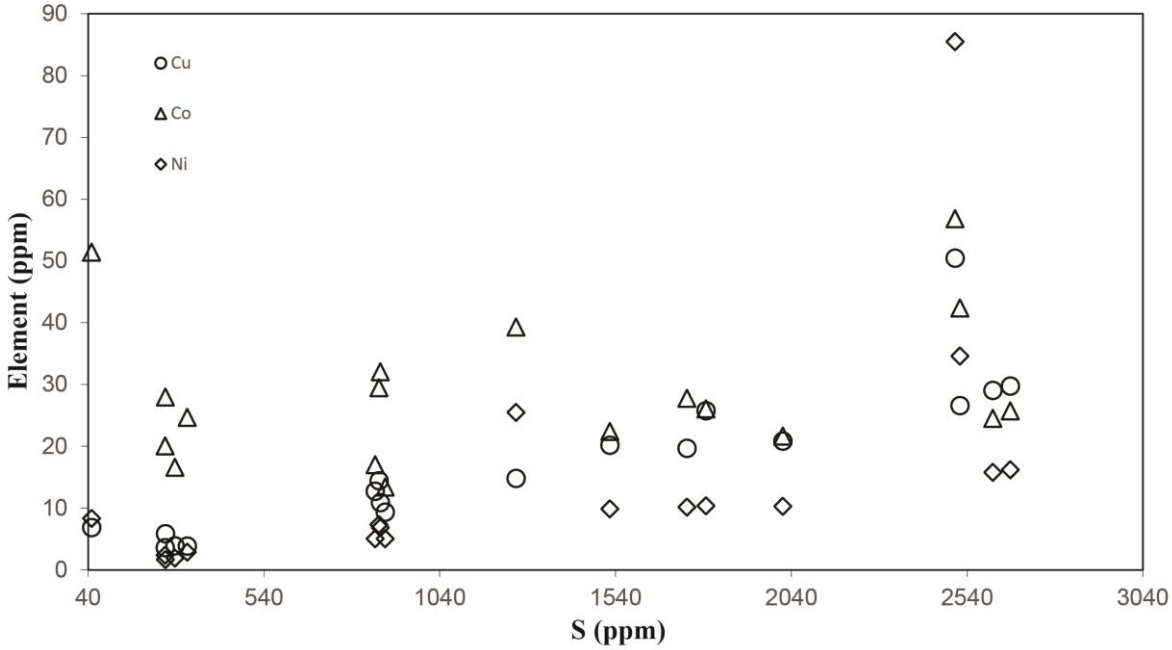

Figure a. Plot of trace transition metal concentrations vs the concentration of S. Note that in general Cu and Co correlation with sulphur value while the correlation is poorer for Ni. Co (triangles), Ni (diamonds), and Cu (curricles).

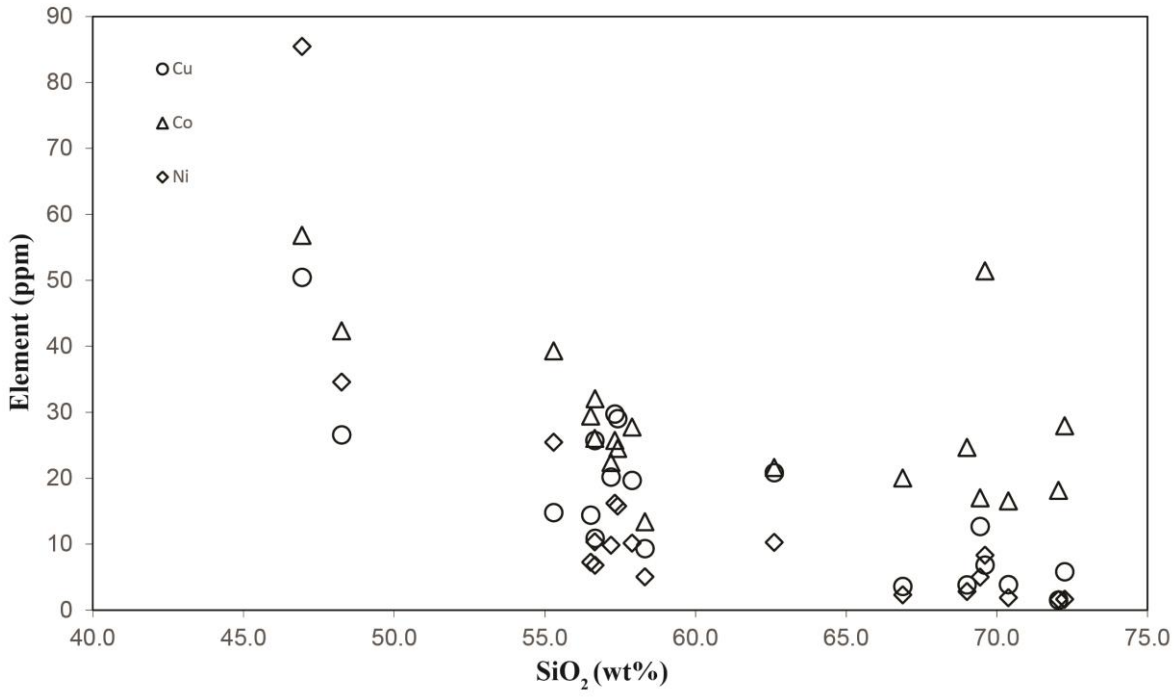

Figure b Plot of trace transition metal concentrations vs the concentration of SiO_2. Note that there is a general inverse correlation for Co (triangles), Ni (diamonds), and Cu (curricles).

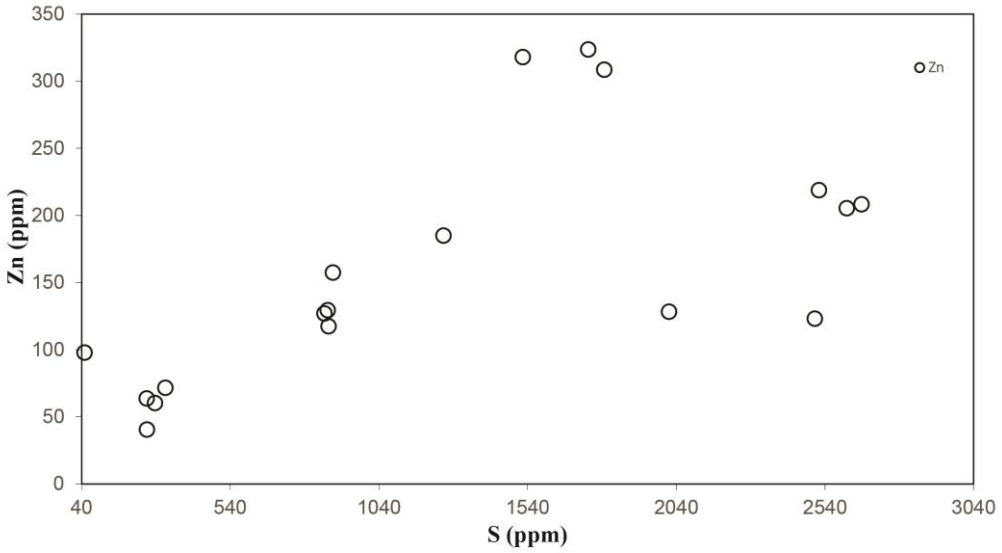

Figure c whole rock Zn concentrations modelled against whole rock S concentration

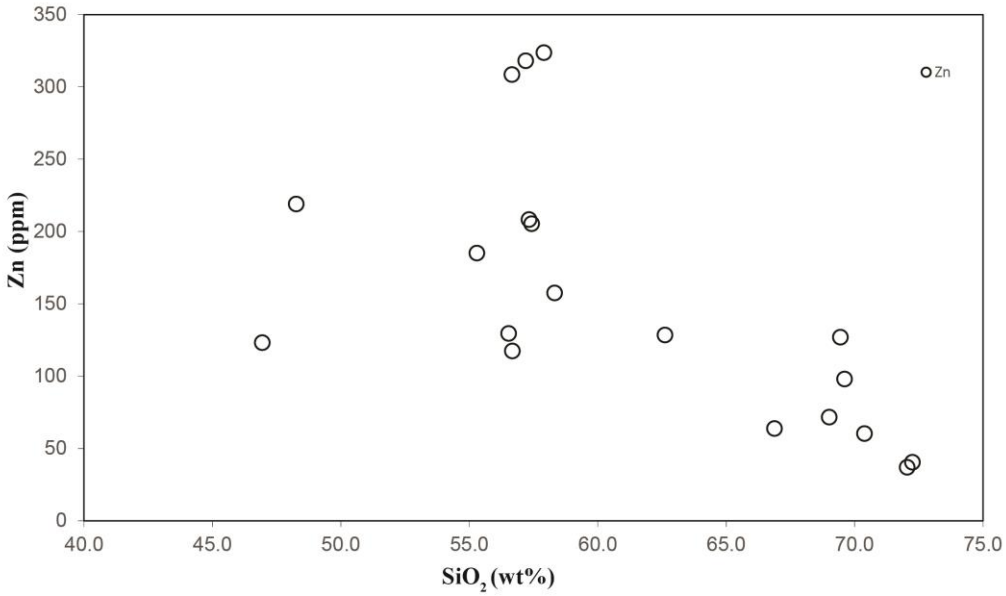

Figure d whole rock Zn concentrations modelled against whole rock SiO_2 concentration.

APPENDIX B

Table 10 EMPA data of pyrite in samples ENCLAVE009 and HYBRID006A

SAMPLE	Fe WT%	Ni WT%	Zn WT%	S WT%	Cu WT%	As WT%	O WT%	TOTAL
009_001 - Pyrite	46.66	0	0	54.15	0.04	0.01	0	100.86
009_001 - Pyrite	46.73	0.17	0	54.10	0	0.06	0	101.06
009_001 - Pyrite	46.63	0	0	54.03	0	0.01	0	100.68
009_001 - Pyrite	45.03	1.47	0	53.92	0.01	0.03	0	100.46
006A_01 6 - pyrite	44.69	0.03	0	53.88	0	0.03	0	98.62
006A_01 6 - pyrite	46.15	0	0	53.56	0	0	0	99.71
006A_01 6 - pyrite	46.32	0	03	53.21	0.02	0.03	0	99.58
006A_01 6 - pyrite	46.45	0.01	0.02	53.64	0	0	0	100.12
009_012 - Pyrite	45.36	0	0	53.53	0	0.04	0	98.93
009_012 - Pyrite	45.44	0	0	53.08	0	0	0	98.51
009_012 - Pyrite	45.74	0	0.01	53.41	0.03	0.07	0	99.26
009_012 - Pyrite	46.17	0.19	0	53.01	0	0.03	0	99.39